

THESIS FOR THE DEGREE OF  
LICENTIATE OF ENGINEERING

---

NEUTRON SCATTERING INVESTIGATIONS  
OF PROTON DYNAMICS IN ACCEPTOR DOPED  
BARIUM ZIRCONATES

Daria Noferini

Department of Physics  
CHALMERS UNIVERSITY OF TECHNOLOGY  
Göteborg, Sweden 2016

# NEUTRON SCATTERING INVESTIGATIONS OF PROTON DYNAMICS IN ACCEPTOR DOPED BARIUM ZIRCONATES

Daria Noferini

©Daria Noferini, 2016

Department of Physics  
Chalmers University of Technology  
SE-412 96 Göteborg, Sweden

This thesis work is part of a collaboration agreement between Chalmers University of Technology and the Institut Laue-Langevin (ILL). It has been financially supported primarily by grants from the Swedish Research Council (grant No. 2010-3519 and 2011-4887) and from the ILL (grant No. ILL1279.1). I have been outstationed at the ILL in Grenoble (France) for most of the time.

Chalmers Reproservice  
Göteborg, Sweden 2016

NEUTRON SCATTERING INVESTIGATIONS OF PROTON DYNAMICS IN  
ACCEPTOR DOPED BARIUM ZIRCONATES

Daria Noferini

Department of Physics  
Chalmers University of Technology

**Abstract**

Hydrogen fuel cells represent one of the most promising sustainable technologies for energy conversion. The advantages of the combination of a solid state electrolyte and low operational temperatures ( $< 750$  °C), not yet achievable, might be enabled by the use of proton conducting solid electrolytes, bringing these devices into everyday life. However, even for the best solid electrolytes available today, the proton conductivities at the desired temperatures remain too low. In this context, a deeper understanding of the proton conduction mechanism in currently available materials is crucial for the development of new materials combining sufficiently high conductivities with good chemical stability.

This thesis presents an investigation of the proton dynamics in barium zirconates, a well-known promising class of proton conducting oxides. It has been shown that the macroscopic proton conductivities differ order of magnitudes depending on the chemical composition of the materials. The aim of the present study is therefore to obtain a detailed description of the atomic scale proton dynamics in the two hydrated proton conducting oxides  $\text{BaZr}_{0.9}\text{M}_{0.1}\text{O}_{2.95}$  ( $M = \text{Y}$  and  $\text{Sc}$ ), and correlate this with the macroscopic proton conductivity of the materials. For this reason, the combination of different neutron spectrometers was exploited to map an extensive dynamical region, and the degree of hydration of the samples was also carefully monitored. In the picosecond time region, we observed localised proton dynamics with low energy barriers, no strong dependence on the type of dopant atoms (Y or Sc), and a spatial geometry compatible

with proton jumping between two neighbouring oxygens or reorientation of the hydroxyl group. Studies over a wide time scale suggest a complex pattern of several dynamics, most likely related to the presence of different proton sites.

**Keywords:** *Proton conductors, perovskites, proton dynamics, neutron scattering, QENS, fuel cells, energy materials*

# Acknowledgments

## Supervisors:

**Maths Karlsson**

Department of Physics, Chalmers University of Technology, Göteborg

and

**Michael M. Koza**

Institut Laue-Langevin, Grenoble.

\* \* \*

Göran Wahnström, Laura Mazzei, Carin Österberg, and Ezio Zanghellini;

Aleksandar Matic.

Department of Physics, Chalmers University of Technology, Göteborg.

Peter Fouquet, Gøran J. Nilsen, Bernhard Frick, Andrew Wildes,

Ingo Hoffmann, Marco Maccarini, Jacques Ollivier, Bela Farago,

Richard Ammer, Markus Appel, Didier Richards, Eric Thaveron,

Dimitry Renzy, Wayne Clancy, Jerome Halbwachs, and Claude Gomez;

Helmut Schober and William G. Stirling.

Institut Laue-Langevin, Grenoble.

Seikh M. H. Rahman and Sten Eriksson.

Department of Chemistry, Chalmers University of Technology, Göteborg.

Wiebke Lohstroh and Zachary Evenson.

Heinz Maier-Leibnitz Zentrum, Technische Universität München, Garching.

Moureen C. Kemei and Ram Seshadri.

University of California, Santa Barbara.

\* \* \*

I wish to extend my gratitude to all those people who are supporting me  
in this “journey”.



*“Come, we shall have some fun now!” thought Alice.*

*“I’m glad they’ve begun asking riddles.”*

Lewis Carroll, *Alice’s Adventures in Wonderland*

*To all the curious people*



# Contents

<b>List of appended papers</b>	<b>iii</b>
<b>Introduction</b>	<b>v</b>
<b>1 Proton conducting oxides</b>	<b>1</b>
1.1 Solid oxide fuel cells . . . . .	1
1.2 Proton conducting perovskites . . . . .	3
1.2.1 Overview and general structure . . . . .	4
1.2.2 Proton conduction in perovskite oxides . . . . .	5
1.2.3 Doping and proton incorporation . . . . .	6
1.2.4 Proton conduction mechanism . . . . .	8
1.2.5 The effect of the dopant atoms . . . . .	11
1.3 Summary of the chapter and remarks . . . . .	13
<b>2 Neutron scattering</b>	<b>15</b>
2.1 Theoretical introduction and basic definitions . . . . .	16
2.2 Polarization analysis and separation of coherent and incoherent components . . . . .	21
2.3 Quasi-elastic neutron scattering . . . . .	22
2.4 Summary of the chapter and remarks . . . . .	23

<b>3</b>	<b>Experimental techniques and application to the study of proton conductors</b>	<b>25</b>
3.1	Time-of-flight spectroscopy . . . . .	27
3.2	Backscattering spectroscopy . . . . .	28
3.3	Spin-echo spectroscopy . . . . .	29
3.4	Neutron diffraction with polarization analysis . . . . .	29
3.5	Summary of the chapter and remarks . . . . .	30
<b>4</b>	<b>Summary of the appended papers</b>	<b>33</b>
4.1.1	Paper I . . . . .	33
4.1.2	Paper II . . . . .	34
<b>5</b>	<b>Conclusions and outlook</b>	<b>37</b>
<b>A</b>	<b>Hydration/dehydration equilibrium</b>	<b>41</b>
A.1	Concentration of protonic defects . . . . .	41
A.2	Details of the calculation of the hydration curves . . . . .	42
<b>B</b>	<b>Instrumentation and data treatment</b>	<b>45</b>
B.1	Time-of-flight spectroscopy . . . . .	45
B.1.1	TOF data treatment . . . . .	47
B.2	Backscattering spectroscopy . . . . .	48
B.2.1	BS data treatment . . . . .	51
B.3	Neutron spin-echo spectroscopy . . . . .	51
B.4	Polarization analysis at D7 . . . . .	54
	<b>Bibliography</b>	<b>57</b>
	<b>Papers I-II</b>	<b>69</b>

# List of appended papers

## **I. Proton dynamics in hydrated $\text{BaZr}_{0.9}\text{M}_{0.1}\text{O}_{2.95}$ ( $M = \text{Y}$ and $\text{Sc}$ ) investigated with neutron spin-echo**

Daria Noferini, Michael M. Koza, Peter Fouquet, Gøran J. Nilsen, Moureen C. Kemei, Seikh M. H. Rahman, Marco Maccarini, Sten Eriksson, and Maths Karlsson.

*Under review in The Journal of Physical Chemistry C*

## **II. Local proton dynamics in hydrated $\text{BaZr}_{0.9}\text{M}_{0.1}\text{O}_{2.95}$ ( $M = \text{Y}$ and $\text{Sc}$ ) investigated by quasi-elastic neutron scattering**

Daria Noferini, Michael M. Koza, and Maths Karlsson.

*In manuscript*



# Introduction

In an energy demanding society, the need of *sustainable technologies* for energy production and conversion becomes more and more essential. Within the different available technologies, a valuable place is occupied by fuel cells. These devices enable to directly convert stored chemical energy from a fuel into usable electrical energy with high efficiency, also reducing, or eliminating, harmful emissions [1,2]. To adapt fuel cells to the different applications, an extreme flexibility in terms of fuels and cell designs would be required, which is achievable using a solid electrolyte [1–4]. Furthermore, solid proton conducting electrolytes may enable the functioning of this kind of devices at lower operational temperatures than what is currently possible (usually higher than 750 °C), additionally extending their range of applications [1,2,5].

However, materials that combine high values of conductivities with a good chemical stability are needed as electrolytes, and at the state of the art an “electrolyte gap” is still present between *ca* 100 °C and 500 °C [6,7]. To tailor these materials with the desired features for applications, it is fundamental to understand the details of the proton conduction mechanism of those materials which show promising characteristics. Hydrated acceptor doped perovskite oxides are considered one of the most interesting class of proton conducting oxides. In particular, barium zirconates combine high proton conductivities with a good chemical stability [7].

To disentangle the proton dynamics in proton conducting oxides, neutron

---

scattering and in particular quasi-elastic neutron scattering emerged among the different experimental techniques, due to the unique features of neutrons as a probe, including a high sensitivity for hydrogen [8, 9].

In this study, neutron scattering techniques have been used to investigate hydrated  $\text{BaZr}_{0.9}\text{M}_{0.1}\text{O}_{2.95}$  ( $M = \text{Y}$  and  $\text{Sc}$ ). The key issue to understand is the influence of the type and concentration of the dopant atom ( $M$ ) on the microscopic proton dynamics and relate it to the large differences in proton conductivities shown by these materials [7].

# Chapter 1

## Proton conducting oxides

Research on solid state proton conductors is currently one of the hottest topics in material science, mainly because of the many technological devices in which they can be applied, especially in the field of “green energy”. Examples are sensors, hydrogen pumps, steam electrolyzers, and fuel cells [7, 10, 11].

A broad range of oxides show proton conduction properties [7, 12, 13]. A not exhaustive list includes phosphates (*e.g.*  $\text{LaPO}_4$  [14]), rare-earth oxides (*e.g.*  $\text{Er}_2\text{O}_3$  [15]), rare-earth ortho-tantalates and niobates (*e.g.*  $\text{LaNbO}_4$  [16]), brown-millerite structured oxides (*e.g.*  $\text{Ba}_2\text{In}_2\text{O}_5$  [17]), pyrochlores (*e.g.*  $\text{La}_2\text{Zr}_2\text{O}_7$  [18]), and oxides with perovskite structure (*e.g.*  $\text{SrZrO}_3$  [19]). This latter class of oxides is of primary interest for applications [11].

### 1.1 Solid oxide fuel cells

Invented in the middle of the 19th century by sir William Grove, fuel cells can be viewed as a cross between a battery and a continuously fuelled, air breathing, device [4, 5]. Fuel cells had one of the first successful applications within the space technologies, for which an electrical energy conversion device capable of

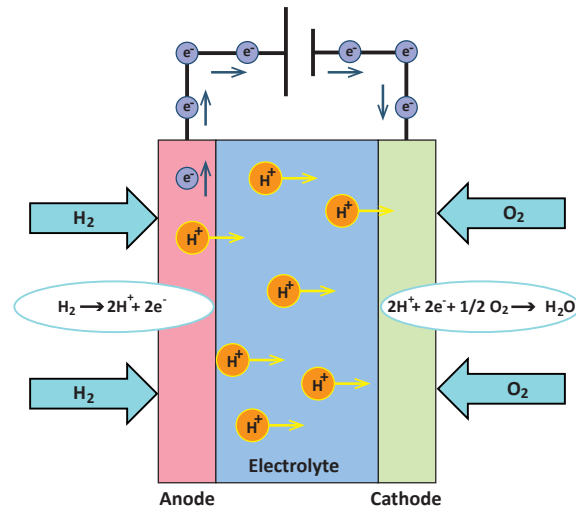


Figure 1.1: Schematic view of a SOFC based on a proton conducting electrolyte

providing electricity, heat and potable water was a convenient improvement in respect to other power sources, such as batteries [4].

The classification of fuel cells is usually done on the basis of their electrolyte material. Fuel cells using a solid oxide electrolyte (Solid Oxide Fuel Cells, SOFCs) are extremely versatile, being capable to oxidise a wide range of fuels such as hydrogen, hydrocarbons or even carbon [1]. The electrolyte is usually an oxide ion conductor, however, depending on the type of fuel cell, it can also be a proton, carbonate or hydroxide ion conductor [5].

The electrolyte is placed between a pair of electrodes. An oxidant, usually oxygen in the form of air, is fed to the cathode, and fuel is supplied to the anode. A scheme of functioning for a SOFC based on a proton conducting electrolyte is shown in Figure 1.1. An advantage of using a proton conducting electrolyte is that water as by-product is produced at the cathode side instead of the anode. This prevents the dilution of the fuel and minimizes the re-oxidation of the anode [20].

The usual operational temperature range for the most used SOFCs, based

on oxygen ion transport, is around 800–1000 °C. As a consequence of this high temperature, these fuel cells have high cell costs, limited endurance, and they exhibit long start up and shutdown cycles, that reduce their applicability in portable power and transportation devices [1, 2, 5]. Although there is not an ideal operating temperature for fuel cells in general, lowering the operation temperature of SOFCs below 650 °C would lead to some important advantages, such as increased life-time up to more than ten years, increased maximum theoretical efficiency, reduced time needed for start up. This would therefore unlock a wide range of potential applications, for example in the transportation market, as mentioned above [1, 2, 5]. Thus, it is not surprising that a large part of solid-state materials research is focused on the improvement of the component materials of SOFCs, to enable their functioning at lower operational temperatures [2]. Considering that the proton has a much smaller size than the oxide ion, higher conduction at lower temperature is envisaged for proton conducting electrolytes [5].

## 1.2 Proton conducting perovskites

A crucial role in the efficiency of proton conducting SOFCs is played by the electrolyte, that needs to transport efficiently the protons from the anode to the cathode. Required conductivities should exceed  $10^{-2}$ – $10^{-1}$  S cm<sup>-1</sup> [21]. Nevertheless, in the operational range of *ca* 100–650 °C, *i.e.* the one of *low-* and *intermediate-temperature* SOFCs,<sup>1</sup> currently available materials do not reach this goal [6]. This “electrolyte gap” constitutes one of the main problems to overcome in order to bring low-temperature and intermediate-temperature SOFCs

---

<sup>1</sup>On the basis of their operational temperature, fuel cells can be also classified into high, intermediate and low-temperature ones. Although their ranges are not universally defined, they indicatively take values of  $T > 750$  °C,  $500$  °C  $< T < 750$  °C,  $T < 500$  °C, respectively [5, 21]

into our everyday life.

Among the currently available proton conductors, proton conducting oxides of perovskite structure have emerged as most promising due to their combination of good chemical stability with high proton conductivities, although yet too low in the range 100–650 °C, where they reach values up to  $10^{-4}$ – $10^{-2}$  S cm<sup>-1</sup> [5,7]. A detailed understanding of the proton conduction mechanism in these materials may bring the essential knowledge for developing new materials with higher conductivity.

### 1.2.1 Overview and general structure

The term *perovskite* originally identifies a calcium titanate mineral, named after the Russian mineralogist Lev Perovski [22]. In a more general way, it is used to refer to a wide class of compounds with general formula  $ABX_3$ , where  $A$  is a larger cation than the cation  $B$ , and  $X$  is an anion, often oxygen. The “ideal” perovskite structure is cubic, with the  $A$  cation and the anions forming a face centred cubic (*fcc*) array, with a large octahedron at the centre of the cell (see Figure 1.2). However, depending on the relative sizes of  $A$  and  $B$ , distortions away from cubic symmetry can occur. An indication on the structure may be obtained using the Goldschmidt factor  $t$  [23], defined as  $t = \frac{r_A+r_O}{\sqrt{2}(r_B+r_O)}$ , where  $r_A$ ,  $r_B$  and  $r_O$  are the ionic radii of  $A$ ,  $B$ , and  $O$ , respectively. It is equal to 1 for an ideal cubic structure.

In this thesis, focused on barium zirconate materials, we will generally refer to “simple”  $ABO_3$ -type perovskites. Further information about the perovskite structure and other, “more complex”, similar materials may be found, for example, in the 2008 review by Davies and co-authors and references therein [24].

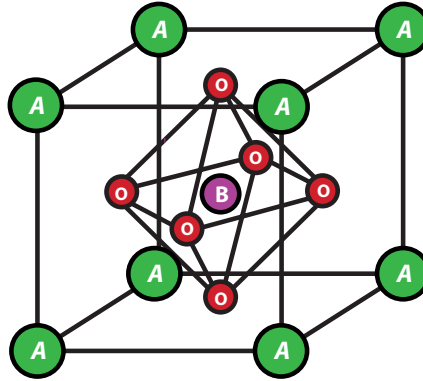


Figure 1.2: Schematic view of a material exhibiting an ideal cubic perovskite structure of general chemical formula  $ABO_3$ . The cation  $A$  is larger than the cation  $B$ .

### 1.2.2 Proton conduction in perovskite oxides

Perovskite oxides started drawing the attentions of the solid-state-ionics community early in the '80ies, when Takahashi and Iwahara first reported proton conduction in the perovskites  $LaYO_3$  and  $SrZrO_3$  [19]. Then, more studies revealed evidence of proton conductivity in a wide range of perovskite materials, covering all combinations of valence of the  $A$  and  $B$  cations [12]. For example, proton conduction was reported in acceptor doped II-IV perovskites, such as  $BaCeO_3$ ,  $BaTbO_3$ , and  $BaZrO_3$ , I-V perovskites, such as  $KTaO_3$ , and III-III perovskites, such as  $LaScO_3$  [12]. The reason for the acceptor doping is to further charge compensation by protons dissolved from water vapour. This will be explained in more detail below.

The high values of proton conductivities make perovskites interesting for different applications, such as fuel cells, hydrogen sensors and steam electrolyzers, as mentioned in the previous section [7, 10, 11]. The requirement for effective use in these applications is a balance among high proton concentration (*i.e.*

a favourable hydration kinetics), high proton mobility, and chemical stability. Generally one of the best combinations of these factors is represented by barium zirconate, especially when doped with yttrium [7].

### 1.2.3 Doping and proton incorporation

Protons are not part of the nominal perovskite structure. In wet atmosphere, protons can enter into the perovskite structure as interstitial defects or compensated by metal vacancies [12]. However, to significantly enhance their presence it is necessary to create oxygen vacancies, which may be then compensated for during an hydration process. A common strategy is to introduce a lower-valent ion into the  $B$ -site, which is called *acceptor doping* [7]. In complex perovskites containing two or more different  $B$ -site cations, vacancies can be formed also varying the ratio of the concentrations of such cations [7, 12]. In the acceptor doping procedure, the acceptors are compensated by oxygen vacancies in the dry state. During the hydration process, water from the gaseous phase dissociates into hydroxide ions and protons; the hydroxide ions fill the oxide ion vacancies and the protons form covalent bonds with lattice oxygens [7]. In the ideal situation, the oxygen vacancy concentration in the dry state is equal to half of the dopant concentration, and the concentration of protonic defects in a fully hydrated sample matches the dopant concentration [7]. A schematic view of the doping and hydration processes for barium zirconate,  $\text{BaZrO}_3$ , is sketched in Figure 1.3.

The hydration/dehydration equilibrium in an acceptor doped solid oxide can be written in Kröger-Vink notation<sup>2</sup> as:



---

<sup>2</sup>We recall that in Kröger-Vink notation, the superscript of a point ( $\bullet$ ) indicates a positive effective charge, and a cross ( $\times$ ) indicates a neutral effective charge.

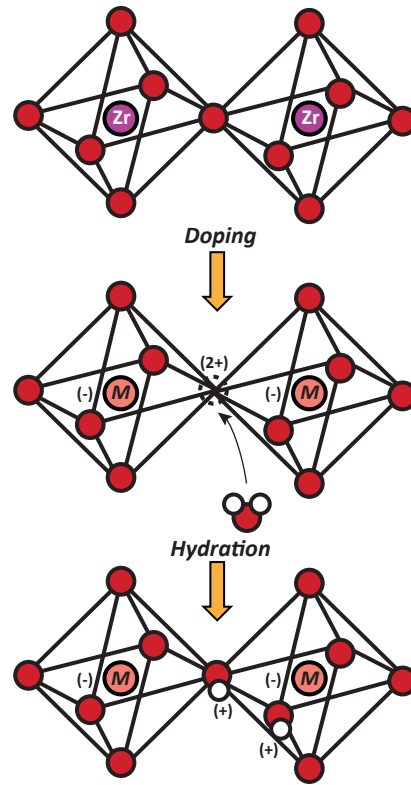


Figure 1.3: Schematic view of the doping and hydration processes for barium zirconate. A lower-valent ion  $M^{3+}$  (e.g.  $Y^{3+}$ ,  $Gd^{3+}$ ...) is inserted into the  $B$ -site occupied by  $Zr^{4+}$ , creating oxygen vacancies. These oxygen vacancies are filled by hydroxide ions coming from the dissociation of water molecules at high temperature, whereas protons form covalent bonds with oxygens of the lattice.

where  $V_{\text{O}}^{\bullet\bullet}$  is the oxygen vacancy,  $\text{O}_{\text{O}}^{\times}$  is the oxide ion, and  $\text{OH}_{\text{O}}^{\bullet}$  is the hydroxyl ion. Making use of thermodynamic quantities and relations, it is possible to calculate the theoretical concentration of protonic defects as [25]:

$$[\text{OH}_{\text{O}}^{\bullet}] = N_{\text{O}} \frac{K'}{K' - 4} \left[ 1 - \sqrt{1 - \frac{K' - 4}{K'} \left( \frac{2[M]}{N_{\text{O}}} - \frac{[M]^2}{N_{\text{O}}^2} \right)} \right], \quad (1.2)$$

where  $N_{\text{O}}$  is the number of oxygen sites per formula unit, which is 3 for a perovskite and  $[M]$  is the dopant concentration.  $K' = p_w K$ , where  $p_w$  is the vapour partial pressure and  $K$  is the equilibrium constant. Details of the derivation are

given in appendix A.1.

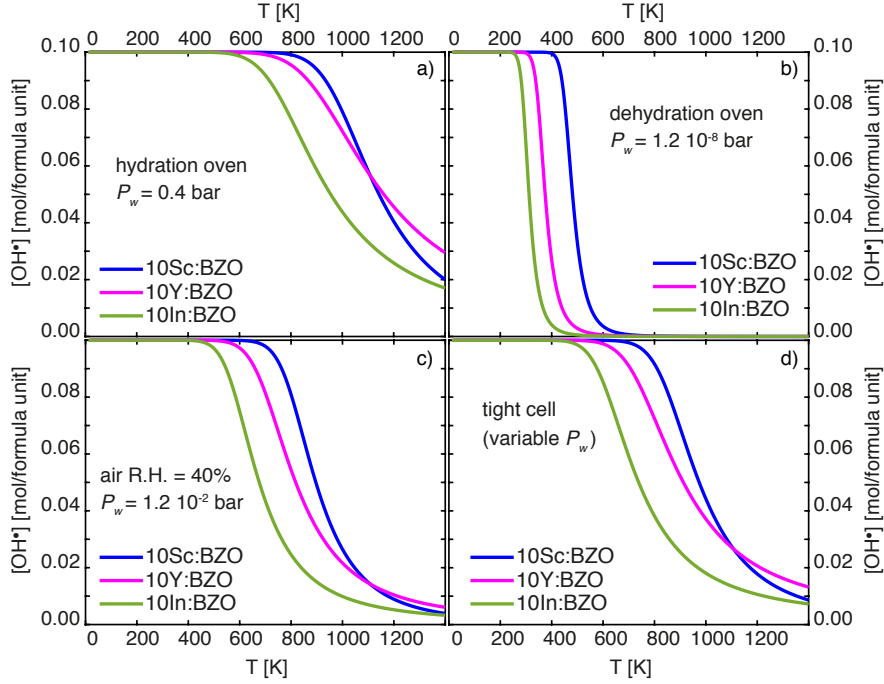


Figure 1.4: Theoretical concentration of protonic defects as a function of temperature for  $BaZr_{0.9}M_{0.1}O_3H_{0.1}$  ( $10M$ :BZO), with  $M = Sc, Y$  and  $In$ . The curves are calculated for: a) hydration procedure; b) dehydration procedure; c) air with 40% relative humidity (R.H.); d) tightly closed cell.

Eq. 1.2 was used to calculate the theoretical concentration of protonic defects as a function of temperature, at relevant conditions for our study. These were used as guidelines during our experimental procedures. Figure 1.4 shows some examples for barium zirconate doped with 10% of Sc, Y or In. Details of their calculation are given in appendix A.2.

### 1.2.4 Proton conduction mechanism

Regarding the proton conduction mechanism in perovskite oxides, since the early studies in the '80ies [26] results from different experiments point towards

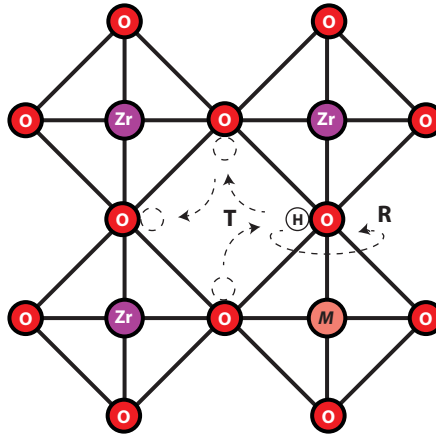


Figure 1.5: Schematic representation of the two elementary steps for proton diffusion in barium zirconate doped with a generic dopant  $M$ : i) proton transfer between neighbouring oxygens (T), and ii) reorientational motion of the  $-OH$  group (R).

a *free proton migration*, as explained in Ref. [27]. The free proton migration involves proton jumping among relatively stationary host anions. This kind of mechanism is termed *Grotthuss mechanism* [28]. A *vehicle mechanism* characterised by proton transport as hydroxide ions moving *via* oxygen vacancies was also considered for these materials, but shelved on the basis of the mentioned experimental evidences [27].

Two elementary steps are supposed to take place within the Grotthuss mechanism: i) proton transfer between neighbouring oxygens, and ii) reorientational motion of the entire hydroxyl group. A schematic representation of the two steps is given in Figure 1.5. Whereas during the first step the breaking of the O-H covalent bond is required, during the reorientation it remains intact, and only its orientation changes. Intuitively, this suggests that reorientation is a relatively rapid process, whilst transfer is the rate-limiting step for long-range proton diffusion. Several studies, conducted with molecular dynamics simulations [29,30],

quasi-elastic neutron scattering [31, 32], muon spin relaxation [33] and infrared spectroscopy [34], support this hypothesis. However, the reorientational motion involves the breaking of hydrogen bonds, and the strong hydrogen bond interactions, manifested by the pronounced red-shifted OH-stretch absorption bands in the infrared spectra, would conversely suggest that rotation can be the rate-limiting step [12, 35]. Some computational studies on cubic perovskites actually suggest that the two processes have similar probability to occur [36, 37]. Indeed, which is the rate-limiting step for proton diffusion has not been elucidated yet. Different investigated systems may lead, perhaps not surprisingly, to different conclusions; yet, even within the same materials an agreement is not reached. In barium zirconates, the materials of concern in this thesis, computational studies generally concluded that the transfer is the slowest step [30, 38, 39]. However, other studies report quite similar activation energies for the two steps [37], at least far from the region of the dopant and far from grain boundaries, where other factors might enter to complicate the description. Conversely, Zhang *et al.* [40] showed that when quantum effects are included in the calculations, the reorientation is the rate limiting step below 600 K. Raiteri *et al.* found an activation energy for transfer almost an order of magnitude lower than that of rotation. In this study, the authors also underline that the activation energy values are very dependent on the functional used, the lattice parameters and the dimension of the supercell [41].

Whereas computational studies have to face discrepancies in results depending on the chosen computational details, experimental ones have to consider the effect on reproducibility introduced by samples prepared with different synthesis routes. In this context, Groß, Beck and collaborators investigated the influence of grain size in hydrated Y-doped barium zirconates using quasi-elastic neutron scattering [42, 43]. Whereas for the microcrystalline material a signal related to a strongly localised hydrogen motion was observed, for the nanosized material

it was hypothesised the presence of a non-structured hydrogen motion in the grain boundary regions or on the surface of the crystallites. How the synthesis route affects the proton motion is presented also in the study of Azad *et al.* [44], where two cubic polymorphs of Y-doped barium zirconates showing different conductivities are obtained by changing the annealing conditions. The possible impact of the hydration degree and presence of different additional hydrogenated species, which may form during the various steps of the synthesis and hydration of the samples, is also debated [45–47].

To conclude this section, it is worth to underline how the host lattice is supposed to play an important role in proton diffusion, affecting especially the transfer step [12, 37, 40, 48, 49]. In fact, it is supposed that lattice vibrations reduce the O-O distance and linearise the bent OH-O hydrogen bond [12], and the concept of “phonon assisted” proton transfer is generally accepted [12, 47, 48, 50, 51]. However, how exactly this coupling should be taken into account in modelling the proton conduction mechanism is not yet unambiguously solved.

### 1.2.5 The effect of the dopant atoms

As seen in section 1.2.3, to permit a significant insertion of protons in the perovskite structures, acceptor doping is commonly used. This procedure clearly leads to local structural and chemical perturbations. One of the main open questions about proton conducting perovskites is the effect of the dopant atom on proton diffusion.

The most commonly shared view is that the dopant atoms act as *traps* for the protons, changing the character of the coordinated oxygens, and making the protons spend longer times in their vicinity before being able to further diffuse. This idea was first introduced by Hempelmann in 1995, on the basis of quasi-elastic neutron scattering data [52]. The two components revealed by the experiment were interpreted as the consequence of two different sites occupied

by the protons, in a trapping and release scenario. Further experimental results obtained with quasi-elastic neutron scattering [51, 53–55], muon spin relaxation [33], and NMR combined with conductivity measurements [56] supported this view. Also several simulation studies confirmed this scenario [30, 37, 41, 48, 57–60].

In a different hypothesis, the dopant acts in a less structural localised fashion. This was proposed on the basis of conductivity measurements, that showed a decreasing proton mobility with increasing doping level, as a result of a generally increased activation energy [36]. However, this second view encountered less support from further studies.

Leaving aside the discussion about a localised trapping behaviour or a less localised effect caused by the dopants, it is not yet clarified the strong influence of the type of dopant atom and its concentration on proton dynamics. Looking for example at the proton diffusion coefficients obtained from conductivity measurements reported for cubic barium zirconates by Kreuer *et al.* [61], it is possible to note that, in spite of their similar structure, different dopant atoms may lead to very different proton mobilities. At 500 °C, a sample doped with 10% of Y shows a diffusion coefficient value of the order of  $10^{-6} \text{ cm}^2 \text{ s}^{-1}$ , *i.e.* one order of magnitude higher than those of samples doped with the same percentage of Sc or In. The same experimental trend found for proton mobility was reproduced by a density functional theory study [37]. Several properties of the dopant ions have been considered to play a significant role: the ionic radius [37, 61, 62], the different character of oxygen-dopant bonding depending on the electronic structure [61–63], and the absolute hardness [64]. Further, quasi-elastic neutron scattering and neutron spin-echo spectroscopy were used to investigate dynamics in barium zirconates with either different dopant atoms or doping level [65, 66]. The quasi-elastic neutron scattering study was done on barium zirconates doped with 10% of Y or Sc [65]. It revealed a local motion with low activation energy and similar relaxation time for the two materials,

which was interpreted as intra-octahedral proton transfer [65]. The spin-echo study focused onto In-doped barium zirconate with a doping level of 10% and 50% [66]. This study suggested a complex dynamical behaviour of the protons for the highly doped material, whereas for the 10% doped material a unique relaxation time related to proton dynamics was observed [66]. However, an unambiguous answer to the effect of the type of dopant is still important object of research.

### 1.3 Summary of the chapter and remarks

In this chapter, the most important features of proton conducting perovskite oxides, a class of material that due to a high proton mobility can be applied in many important technological devices such as SOFCs, have been briefly reviewed.

The acceptor doping followed by an hydration procedure enables the introduction of protons in the structure. The proton conduction mechanism is supposed to take place with a Grotthuss mechanism that can be divided in two elementary steps: transfer and reorientation. A detailed knowledge about the mechanism is still object of active research, and indeed it constitutes a key factor in the development of new materials with higher proton conductivities. Many aspects seem to play an important role: the type of dopant atoms, the stiffness of the oxygen sublattice, the doping and hydration level, the size of the crystals *etc.*

This thesis focuses onto proton dynamics in acceptor doped barium zirconates, notably hydrated  $\text{BaZr}_{0.9}\text{M}_{0.1}\text{O}_{2.95}$  ( $M = \text{Y}$  and  $\text{Sc}$ ). In the cubic symmetry, preserved at low doping values, the oxide ion sites are equivalent, and therefore a possible trapping effect of the dopant atoms should be clearer. Moreover, also the local distortions introduced by the presence of the dopant are

### 1.3 Summary of the chapter and remarks

---

shown to be small, at low doping level, in these systems [67–69]. The dopants were also chosen for the large difference in conductivity of the materials. Within the group of proton conducting barium zirconates, the yttrium-doped material shows the highest conductivity, whereas the scandium-doped shows one of the worst.

## Chapter 2

# Neutron scattering

Neutron scattering is an extremely relevant experimental method for materials science. In particular, a favourable cross section makes neutron scattering particularly suitable for the investigation of the dynamics in materials containing hydrogen.

A comprehensive introduction on neutron scattering is beyond the aim of this thesis. The focus of this chapter will rather be on the basic concepts to follow the interpretation of the measurements. First, the general formalism to describe the outcome of a neutron scattering experiment will be introduced. Then, the features of quasi-elastic neutron scattering will be presented. The quasi-elastic regime is where diffusing or reorientating particles leave the signature of their dynamics, and for this reason quasi-elastic neutron scattering is the main technique used in this study. A short section about the advantages of the use of polarized neutrons will be also given. Polarized neutron diffraction was used to determine the hydrogen concentration in the materials under our investigation.

A more extensive treatment of neutron scattering can be found in Ref. [70–72], which are the main references in this chapter, if not otherwise indicated. The

needed notions of quantum mechanics can be found, for example, in Ref. [73].

## 2.1 Theoretical introduction and basic definitions

Neutrons can be produced and moderated to have energies that match the range of excitations in condensed matter and wavelengths comparable with interatomic distances. Being uncharged, they can easily penetrate the matter. The interaction between neutrons and matter is weak, thus the physical and chemical properties of the samples are not perturbed by the probe. Neutrons are therefore a unique probe for the investigation of both the atomic structure and dynamics in condensed matter.

The interaction of neutrons with the atoms of the sample is directly with the nuclei (*via* the strong nuclear force) and with the magnetic moment of the electrons (*via* the magnetic moment of the neutron). The case of magnetic scattering is of no relevance for the investigated materials, and therefore it will not be treated in the discussion hereafter. The nuclear interaction has a very short range, orders of magnitude smaller than the wavelength of the neutron. As a consequence, the leading term in the neutron-nucleus interaction is of s-wave character, and higher order terms are negligible. It can be therefore characterized by a single parameter,  $b$ , called the scattering length. This quantity varies randomly with the atomic number, and depends also on the mass number and the spin state of the neutron-nucleus system.

In the scattering experiment, the incoming neutron is represented by a plane wave characterized by a wave vector  $\mathbf{k}_i$ . Its magnitude  $k_i$  defines the initial wavelength  $\lambda_i = 2\pi k_i^{-1}$ . The energy of the incident neutron is:

$$E_i = \frac{\hbar^2 k_i^2}{2m_n}, \quad (2.1)$$

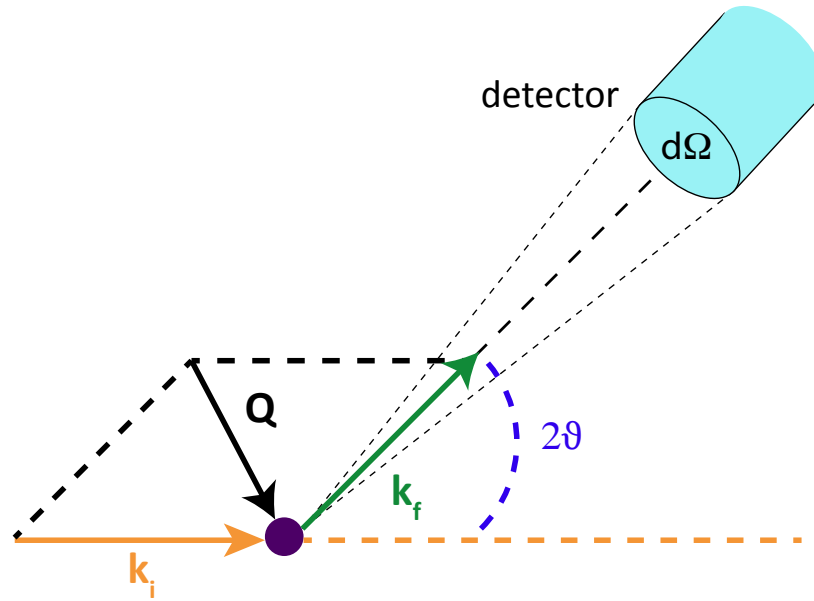


Figure 2.1: Schematic representation of the scattering experiment, and relations among the initial and final wavevectors  $\mathbf{k}_i$  and  $\mathbf{k}_f$  and the scattering vector  $\mathbf{Q}$ .  $2\vartheta$  is the scattering angle, and  $d\Omega$  is the collection solid angle of the detector.

where  $m_n$  is the neutron mass and  $\hbar$  is the reduced Planck constant. Figure 2.1 shows the relationship among the initial wavevector, the final wavevector  $\mathbf{k}_f$  and the scattering vector, defined as

$$\mathbf{Q} = \mathbf{k}_i - \mathbf{k}_f. \quad (2.2)$$

The momentum and energy conservation implies that the momentum transfer from the neutron on the sample is  $\hbar\mathbf{Q}$  and the energy transfer is:

$$\Delta E = E_i - E_f, \quad (2.3)$$

where the final energy  $E_f$  can be derived from the magnitude of the final vector  $k_f$  in analogy to Eq. 2.1. In this definition of the energy transfer, a positive value of  $\Delta E$  corresponds to neutron energy loss. The magnitude of the scattering

vector can be expressed as:

$$Q^2 = k_f^2 + k_i^2 - 2k_i k_f \cos 2\vartheta = \frac{2m_n}{\hbar^2} \left( 2E_i - \Delta E - 2\sqrt{E_i(E_i - \Delta E)} \cos 2\vartheta \right), \quad (2.4)$$

where  $2\vartheta$  is the scattering angle between the incident and scattered wavevectors. For elastic scattering ( $\Delta E = 0$ ), or for scattering processes where  $|\Delta E| \ll E_i$ , the magnitude of the scattering vector can be simplified to

$$Q_{el} = \frac{4\pi}{\lambda_i} \sin \vartheta. \quad (2.5)$$

From Eq. 2.4, it is clear that the region of the energy-momentum transfer space which can be explored during a neutron scattering experiment is limited, and it depends on the initial energy of the neutrons and the minimum and maximum angle that can be probed during the experiment. Figure 2.2 shows a representation for an initial wavelength of 3 Å.

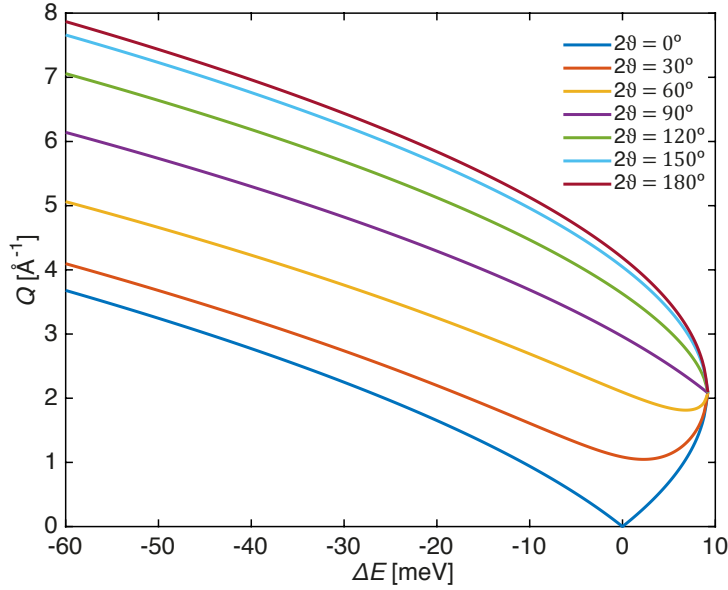


Figure 2.2: Accessible dynamic range for a neutron beam with  $\lambda_i = 3$  Å, for fixed scattering angle. All regions outside the lines for  $2\vartheta = 0^\circ$  and  $2\vartheta = 180^\circ$  are not attainable.

In a neutron scattering experiment, the measured intensity is proportional to the double differential cross section, which gives the fraction of neutrons of incident energy  $E_i$  scattered within the space defined by the differential solid angle  $d\Omega$  and having a final energy in the interval  $[E_f, E_f + dE_f]$ . Within the Born approximation, it takes the form:

$$\frac{d^2\sigma}{d\Omega dE_f} = \frac{k_f}{k_i 2\pi\hbar} \sum_{ij} \bar{b}_i^* \bar{b}_j \int \langle e^{-i\mathbf{Q}\cdot\mathbf{r}_i(0)} e^{i\mathbf{Q}\cdot\mathbf{r}_j(t)} \rangle e^{-i\omega t} dt, \quad (2.6)$$

where the angular brackets denote a thermal average, the horizontal bar represents an average over nuclear spin orientation and distributions, and  $\mathbf{r}_i(t)$  is the position of the scatterer  $i$  at time  $t$ . Considering a monoatomic target, the summation in Eq. 2.6 can be split into a part concerning the time correlations between  $N$  different scatterers ( $i \neq j$ ) and one for self-correlations ( $i = j$ ), obtaining:

$$\frac{d^2\sigma}{d\Omega dE_f} = \frac{k_f}{k_i 2\pi\hbar} \left[ \sum_{i \neq j} \bar{b}^2 \int \langle e^{-i\mathbf{Q}\cdot\mathbf{r}_i(0)} e^{i\mathbf{Q}\cdot\mathbf{r}_j(t)} \rangle e^{-i\omega t} dt + \sum_i \bar{b}^2 \int \langle e^{-i\mathbf{Q}\cdot\mathbf{r}_i(0)} e^{i\mathbf{Q}\cdot\mathbf{r}_i(t)} \rangle e^{-i\omega t} dt \right] \quad (2.7)$$

We now introduce the coherent and incoherent dynamic structure factors, respectively:

$$S_{\text{coh}}(\mathbf{Q}, \omega) = \frac{1}{2N\pi\hbar} \sum_{ij} \int \langle e^{-i\mathbf{Q}\cdot\mathbf{r}_i(0)} e^{i\mathbf{Q}\cdot\mathbf{r}_j(t)} \rangle e^{-i\omega t} dt \quad (2.8)$$

$$S_{\text{inc}}(\mathbf{Q}, \omega) = \frac{1}{2N\pi\hbar} \sum_i \int \langle e^{-i\mathbf{Q}\cdot\mathbf{r}_i(0)} e^{i\mathbf{Q}\cdot\mathbf{r}_i(t)} \rangle e^{-i\omega t} dt; \quad (2.9)$$

and the coherent and incoherent scattering cross section:

$$\sigma_{\text{coh}} = 4\pi \bar{b}^2 \quad (2.10)$$

$$\sigma_{\text{inc}} = 4\pi (\bar{b}^2 - \bar{b}^2). \quad (2.11)$$

We can therefore rewrite Eq. 2.7 as:

$$\frac{d^2\sigma}{d\Omega dE_f} = \frac{Nk_f}{4\pi k_i} [\sigma_{\text{coh}}S_{\text{coh}}(\mathbf{Q}, \omega) + \sigma_{\text{inc}}S_{\text{inc}}(\mathbf{Q}, \omega)] \quad (2.12)$$

The coherent scattering gives interference effects. It depends on the correlation between the positions of the same nucleus at different times, and on the correlation between the positions of different nuclei at different times. It is proportional to the squared average of the scattering length. Its intensity presents a strong anisotropy. For example, if we consider elastic scattering in crystals, intensity peaks appear for the particular directions of the scattered beam that satisfy the Bragg condition. The incoherent scattering depends on the correlation between the positions of the same nucleus at different times, and it is proportional to the standard deviation of scattering lengths in the system.

The time Fourier transforms (FTs) of the coherent and incoherent dynamic structure factor give respectively the coherent and incoherent intermediate scattering function  $I_{\text{coh}}(\mathbf{Q}, t)$  and  $I_{\text{inc}}(\mathbf{Q}, t)$  [74]. These functions are the space FTs respectively of the pair and self correlation function  $G(\mathbf{r}, t)$  and  $G_s(\mathbf{r}, t)$ . The pair correlation function describes the probability of observing any particle at distance  $\mathbf{r}$  and after a time  $t$  in relation to the position of a given particle at  $t = 0$ . The self correlation function gives the probability of finding exactly the same particle at distance  $\mathbf{r}$  and after time  $t$ . A diagram describing the relationships within these different functions and their accessibility by different methods is given in Figure 2.3.

Finally, we note that the particularly large incoherent scattering cross section of hydrogen makes neutron scattering notably suitable for the study of proton self-diffusion, enabling the investigation even in materials with relatively low amounts of protons, such as the proton conductors investigated in this thesis. Table 2.1 summarises the cross sections for the different atoms in the investigated materials.

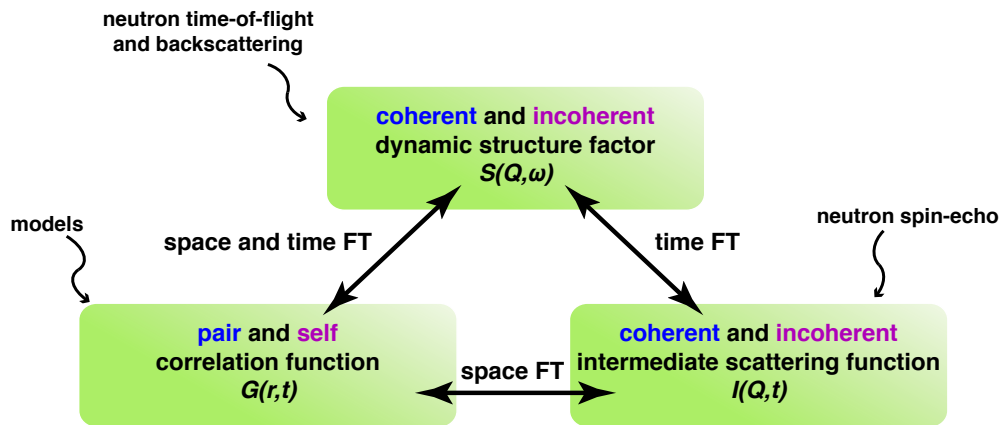


Figure 2.3: Relationship between different functions used in neutron scattering. The functions are related to each other by time and/or space Fourier transformations (FTs).

## 2.2 Polarization analysis and separation of coherent and incoherent components

The statistical distribution of nuclear scattering lengths can have its origin in the atomic isotopes or in the nuclear spin. This implies two contributions for the incoherent scattering: spin-incoherent and isotope-incoherent [75]. Coherent scattering and isotope incoherent scattering do not change the spin state of the neutron, *i.e.* they are non-spin-flip processes [76,77]. Spin-incoherent scattering, conversely, has a probability of 2/3 to change the spin state of the neutron. Polarized neutrons, *i.e.* neutrons all having the same spin vector, can be therefore used to separate the different scattering contributions [76–79]. In the case of non-magnetic samples, to obtain the separation of the nuclear (coherent and isotope incoherent) and spin-incoherent contribution, it is sufficient to measure the total spin-flip and non-spin-flip cross sections [76–79]. If instead magnetic scattering is present, the technique that provides an unambiguous separation

## 2.3 Quasi-elastic neutron scattering

---

Element	$\sigma_{scatt}$	$\sigma_{coh}$	$\sigma_{inc}$	$\sigma_{abs}$
	[barn]	[barn]	[barn]	[barn]
H	82.03	1.7568	80.27	0.3327
O	4.233	4.233	0.0008	0.00019
Sc	23.6	19.0	4.5	27.5
Y	7.71	7.55	0.16	1.28
Zr	6.46	6.44	0.02	0.185
In	2.62	2.08	0.54	193.8
Ba	3.38	3.23	0.15	1.1

Table 2.1: Scattering (coherent and incoherent) and absorption cross sections for the elements composing the materials used in this study. 1 barn =  $10^{-28}$  m<sup>2</sup>.  $\sigma_{scatt}$  is the total scattering cross section. Absorption cross sections are reported for  $\lambda_i = 1.798$  Å. All the values are taken from Ref. [75].

of nuclear, spin-incoherent and magnetic scattering cross sections on a multi-detector neutron spectrometer is called *xyz*-polarization analysis, and it is explained in detail in Ref. [79]. Summarising, the spin-flip and non-spin-flip cross sections are measured for three orthogonal orientations of the neutron beam polarization. From linear combinations of these, the nuclear, spin incoherent, and magnetic contributions are extracted.

## 2.3 Quasi-elastic neutron scattering

Diffusing or reorientating particles in the sample exchange small amounts of energy with neutrons. As a result, the elastic peak is broadened by a continuous distribution of energies, the *quasi-elastic* component, characterized by its width at half maximum. This broadening in the momentum-energy transfer phase-space translates equivalently into a decay of the intermediate scattering function

in the momentum transfer-time domain. Typical energies for the quasi-elastic contribution are in the orders of meV or  $\mu\text{eV}$ , corresponding to a time window of roughly  $10^{-10}$ – $10^{-12}$  s. Faster motions, out of the quasi-elastic window, give rise to features at higher exchanged energies, *i.e.* the inelastic components. A sketch of the elastic, inelastic and quasi-elastic scattering components in a spectrum is given in Figure 2.4.

An accurate investigation of the shape of this quasi-elastic component, and of the dependency of the broadening (or analogously of the time decay) on the momentum transfer, yields information on the physical nature of the motions of the scatterers [80,81]. Finally, in the case of localised or confined motion, the analysis of the  $Q$ -dependence of the relative amplitudes of the elastic and quasi-elastic components gives insights into the geometry of the dynamics [80,81].

Quasi-elastic neutron scattering (QENS) is the neutron scattering technique that surveys the energy window typical of the quasi-elastic broadening, whereas the space window reaches the atomic scale (0.1–10 Å).

## 2.4 Summary of the chapter and remarks

Due to the unique features of neutrons and to the possibility of tuning their energy, neutron scattering can provide useful information about the structure and dynamics in materials. In particular, the good match of length scale and exchanged energies probed by QENS, in addition to the favourable incoherent hydrogen cross section, makes this technique particularly suitable for investigating the dynamical processes of interest of this study [8], and it was hence the main technique used.

To extensively map different time and length scales, the use of various experimental methods and instruments is needed. This will be clarified in the next chapter.

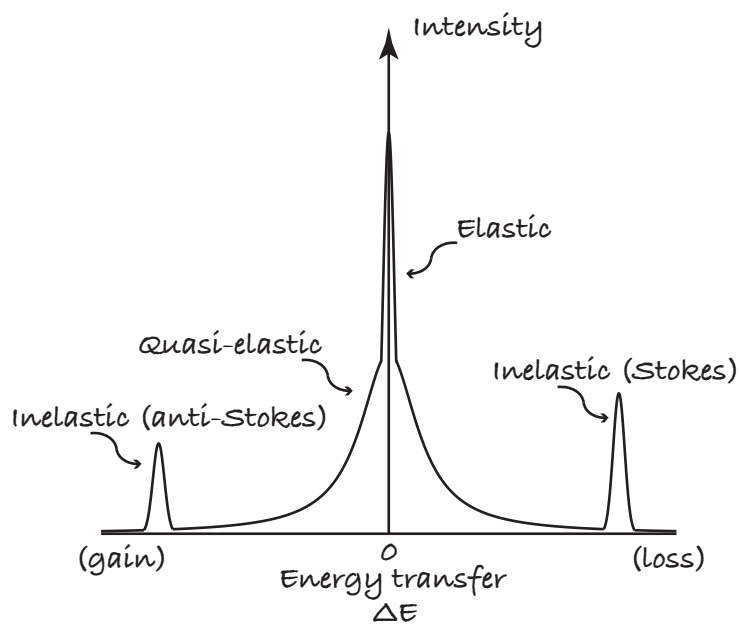


Figure 2.4: Sketch of the elastic, quasi-elastic and inelastic component in a neutron scattering spectrum. According to the definitions given in section 2.1, *gain* and *loss* refer to neutron energy gain and neutron energy loss, respectively.

## Chapter 3

# Experimental techniques and application to the study of proton conductors

Having briefly reviewed the theoretical aspects of neutron scattering of main importance for this thesis, here the focus is moved onto the technical part. Different neutron techniques give access to different time and length scales, therefore providing information that are complementary to each other. Figure 3.1 gives a glance over the many different materials and systems that can be studied within the ranges covered by neutron scattering methods, which are highlighted as polygons in bright colours and shown together with other complementary experimental techniques.

Time-of-flight (TOF), backscattering and spin-echo spectroscopy are the main experimental techniques used in this study. Hereafter they will be briefly described, underlining why they are useful in the investigation of proton conducting materials. Additional information and the schemes of some of the used instruments can be found in Appendix B.

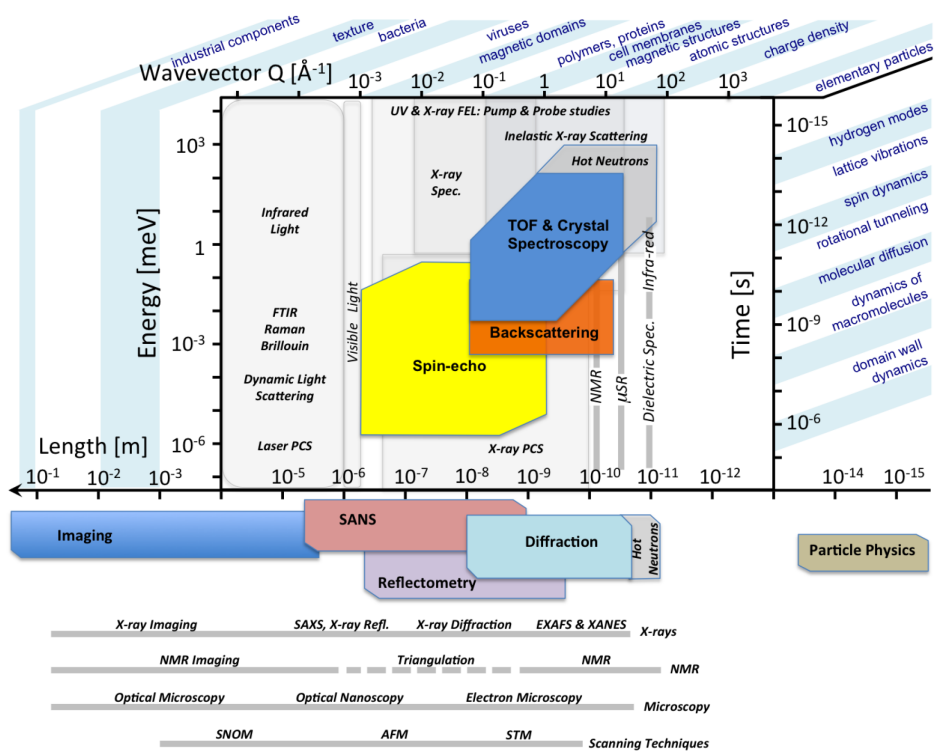


Figure 3.1: Phase-space coverage of different neutron scattering techniques. The various neutron scattering methods provide information about the properties and behaviour of many different materials and systems. The horizontal axes indicate real and reciprocal length scales, whereas the vertical axes refer to time and energy scales. Along the edges, scientific areas falling within different length and time scales are indicated. The experimentally accessible areas of the various neutron-based techniques are shown as polygons in bright colours. A selection of complementary experimental techniques is shown in grey. Figure taken from Ref. [82], courtesy of Arno Hiess.

### 3.1 Time-of-flight spectroscopy

In the TOF method, the neutron is considered as a classical particle, and its energy is determined by measuring the time that it needs to cover a known distance. If a neutron with mass  $m_n$  is travelling over a distance  $L$  in a time  $\Delta t$ , it is possible to express its kinetic energy as:

$$E = \frac{1}{2}m_n v^2 = \frac{h^2}{2m_n \lambda} = \frac{m_n L^2}{2\Delta t^2}, \quad (3.1)$$

where  $\lambda$  and  $v$  are respectively the wavelength and velocity of the neutron and  $h$  is the Planck constant. If during the scattering event the neutron wavelength changes, due to inelastic scattering, this will correspond to a change of the velocity and therefore of the time-of-flight of the scattered neutron [80, 83].

In the TOF instruments, the energy resolution is determined by the wavelength dispersion of the incoming neutron pulse, which depends on the dimension of the opening and the rotating speed of the chopper, and by the uncertainty related to the flight path, which includes the beam divergence, the thickness of the sample, and the detector size. Increasing the resolution is therefore paid with a loss of intensity [83–85]. To achieve high resolution, long wavelengths are required, which consequently strongly limits the maximum achievable  $Q$ .

On the other hand, one of the main strengths of the TOF spectrometers is their great flexibility in choosing the energy resolution (1  $\mu\text{eV}$  – 1  $\text{meV}$ ) and the energy and momentum transfer range, adapting to many different experimental needs [83–85].

In the study of proton conductors, QENS at TOF instruments can provide information on the fundamental steps of the diffusion: transfers between neighbouring oxygens and reorientations. Moreover, the wide dynamical range of these instruments can be used to simultaneously explore the inelastic spectrum in the vibrational range.

## 3.2 Backscattering spectroscopy

In a backscattering (BS) spectrometer, the energy analysis of the scattered neutrons and the monochromatization of the incoming beam are done by single crystals, used in backscattering geometry, *i.e.* with scattering angle  $2\vartheta \approx 180^\circ$  [83, 84, 86]. The backscattering geometry is crucial to achieve high energy resolution, which is improved by one or two orders of magnitude in respect to the TOF instruments while maintaining a broad  $Q$ -range, therefore allowing to study processes in a time scale up to some nanoseconds. BS instruments, in addition to full energy transfer spectra, give the possibility to do fixed window scans at a chosen energy transfer<sup>1</sup> as a function of temperature. These measurements provide an overview on the sample dynamics with good statistics in relatively short measurements. The energy transfer range in these instruments is however typically limited to a few tens/hundreds of  $\mu\text{eV}$  [87, 88].

Investigating the dynamics in proton conductors, the high resolution of BS spectrometers can provide information at longer times in respect to a TOF instrument, possibly enabling the observation of the proton long-range diffusion, especially if measuring at sufficiently low  $Q$ . Moreover, the quick overview on the temperature dependence of the motion given by the fixed window scans can add useful information, for example identifying the onset of a specific process or enabling an accurate estimation of the mean square displacement.

---

<sup>1</sup>Normally it is only possible to have these measurements at  $\Delta E = 0$ , *i.e.* elastic fixed windows scans, but the new BS spectrometers IN16b at the ILL allows also to perform inelastic fixed scans, as explained in Appendix B.2.

### 3.3 Spin-echo spectroscopy

As seen, in the “classic” inelastic spectrometers the improvement of the instrumental resolution, and therefore the maximum time scale that can be probed, can be achieved only at the expense of the intensity. The neutron spin-echo technique (NSE) was introduced to overcome this conflict, pushing the achievable time scales towards longer values [89]. One of the main strengths of NSE is indeed its wide dynamical range. This is possible by encoding the velocity change of incident and scattered neutrons using the Larmor precession of the neutron spin in an external magnetic field, which is used as an “internal clock” [89–91]. An additional peculiarity of NSE is that it directly provides data in the  $(\vartheta, t)$  phase space [91]. A brief description of the basic relations of the technique is given in Appendix B.3.

NSE has been recently applied to explore the proton dynamics in barium zirconates in the ns time scale [92]. It clearly offers a unique possibility to map a wide dynamical region, possibly observing the long-range diffusion in these materials. However, it also presents some drawbacks linked to the characteristics of the technique and the prevalently incoherent nature of the scattering in these materials. They are discussed in more detail in Appendix B.3.

### 3.4 Neutron diffraction with polarization analysis

The hydrogen content of a hydrogenated material can be measured using its spin-incoherent cross section, measured in absolute units. As seen in the previous chapter, the spin-incoherent component can be separated from the nuclear and, in case, magnetic components by  $xyz$ -polarization analysis. Once that the

### 3.5 Summary of the chapter and remarks

---

spin-incoherent cross section  $\left(\frac{d\sigma}{d\Omega}\right)_{\text{si}}$  is obtained in absolute units, its hydrogen-contribution  $\left(\frac{d\sigma}{d\Omega}\right)_{\text{si}}^{\text{H}}$  is derived by subtracting the contribution of the other atoms:

$$\left(\frac{d\sigma}{d\Omega}\right)_{\text{si}}^{\text{H}} = \left(\frac{d\sigma}{d\Omega}\right)_{\text{si}} - \sum_{i \neq \text{H}} \frac{\sigma_{\text{si}}^i n^i}{4\pi}, \quad (3.2)$$

where  $\sigma_{\text{si}}^i$  is the spin-incoherent cross section of the  $i$ -th element in the compound, weighted for its stoichiometric factor  $n^i$ . The result is then divided by  $\frac{\sigma_{\text{si}}^{\text{H}}}{4\pi}$ , yielding the hydrogen molar content per formula unit.

In the study of proton conductors, this technique can be applied to estimate the hydrogen concentration with a good precision (*ca* 10%). Its strength lies in its non-destructiveness, so that the estimation can be done on the very same sample used for other measurements. Our measurements of polarised neutron diffraction (ND) were done at the diffuse scattering spectrometer D7 [79, 87] at ILL, whose scheme is depicted in Appendix B.4. In the case of our materials, the spin-incoherent cross sections can be very well approximated by the incoherent ones [75].

### 3.5 Summary of the chapter and remarks

To conclude this chapter, we note that all the presented experimental techniques have their strengths and limitations. Combining them in a systematic study is therefore crucial to gain new insights into the proton conduction mechanism. QENS measurements on TOF spectrometers of proton conducting materials can give insights into the fundamental steps of the diffusion, *i.e.* the transfer between neighbour oxygens and the reorientation of the -OH group described in Chapter 1. Due to the wide dynamical range of these instruments, within the same measurement also information about the vibrations at relatively low energy can be obtained. NSE and BS spectrometry can provide information at longer times, possibly enabling to observe the proton long-range diffusion, if

measuring at sufficiently low  $Q$ -values.

A good sample characterization is also very important, as well regarding the hydration level in the materials. Neutron polarization analysis can provide the hydrogen concentration with good precision and in a non-destructive measurement.

To underline the importance of combining different techniques, in Table 3.1 we report the main neutron scattering measurements performed within this study<sup>2</sup>, although not all the results will be discussed in this thesis.

---

<sup>2</sup>About 75 days of beamtime, in total.

Method	Instrument	$\lambda_i$ [Å]	Resolution <sup>a</sup> [µeV]	$Q_{el}$ -range [Å <sup>-1</sup> ]	Samples
<sup>†</sup> NSE	IN11	5.5	1.3 ns	0.1–1.2	10Sc:BZO, 10Y:BZO, BZO, 10Sc:BZO*, 10Y:BZO*
NSE	IN11	8.0	4 ns	0.5–0.84	10Y:BZO
TOF	TOFTOF	2.5	440	0.36–4.7	10Sc:BZO, 10Y:BZO, <i>x</i> In:BZO ( <i>x</i> =10, 15, 20)
TOF	TOFTOF	8.0	23	0.1–1.5	<i>x</i> In:BZO ( <i>x</i> =10, 15, 20)
TOF	IN6	4.14	160	0.3–2.6	10Y:BZO, 10Sc:BZO, BZO
<sup>†</sup> TOF	IN5	2.5	620	0.02–4.6	10Sc:BZO, 10Y:BZO
TOF	IN5	8.0	20	0.006–1.4	10Sc:BZO, 10Y:BZO
BS	IN16b	6.3	12	0.2–1.9	10Sc:BZO, 10Y:BZO, <i>x</i> In:BZO ( <i>x</i> =10, 15, 20, 25), BZO
NSE	IN15	8	72 ns	0.05–0.6	10In:BZO, 10In:BZO <sub><i>del</i></sub>
<sup>†</sup> polarised ND	D7	4.8		0.2–2.5	all the previously listed samples

Table 3.1: Summary of the main neutron scattering experiments carried out within this study. All the listed instruments are at the Institut Laue-Langevin (ILL) in Grenoble, France, with the exception of TOFTOF, which is an instrument of the Forschungs-Neutronenquelle Heinz Maier-Leibnitz (FRM II) in Garching, Germany. Samples are indicated as  $xM$ :BZO, where  $x$  is the doping level in percent and  $M$  is the dopant atom. BZO refers to the undoped barium zirconate. Samples marked with \* have a different hydration level in respect to the correspondent non marked ones. The sample marked as *del* has been hydrated and then heated to *ca* 900 °C. The results presented in this thesis were obtained during the experiments marked with <sup>†</sup>.

<sup>a</sup>Full width at half maximum; for NSE the max Fourier time is reported

# Chapter 4

## Summary of the appended papers

### 4.1.1 Paper I

In this paper we have investigated hydrated  $\text{BaZr}_{0.9}\text{M}_{0.1}\text{O}_{2.95}$  ( $M = \text{Y}$  and  $\text{Sc}$ ), in order to understand the effect of temperature, momentum transfer, degree of protonation and dopant atom  $M$  on the present proton dynamics. The chosen setup at the IN11C neutron spin-echo spectrometer allowed to explore a time range of 5 ps–1.3 ns and a momentum transfer range of 0.69–1.23  $\text{\AA}^{-1}$ . The investigation was conducted in a temperature range of 249–563 K. The dynamical range and the high resolution of the NSE spectrometer were chosen with the aim to investigate the long-range diffusion of the protons in the material. The hydration degree of the samples was carefully measured with thermogravimetric analysis and polarised neutron diffraction. In addition, infrared spectroscopy was used to obtain insights into the nature of proton sites.

The results show the presence of pronounced proton motions for temperatures above 300 K, at the time scale accessible by the measurements. In the investigated range, the dynamics do not appear strongly dependent on the  $Q$ -value, suggesting localised motions. Also no strong dependence on the type of

---

dopant atom was observed. The profile of the intermediate scattering function appears very stretched, most likely due to a distribution of different time scales, reflecting the wide distribution of locally different proton configurations shown by the infrared measurements. The footprint of the proton dynamics is suggested to be extended to much longer times, towards the time domain of oxygen diffusion, making the time window probed by our experiment too narrow for a reliable parametrization of the intermediate scattering function. However, the possible presence of immobile hydrogens could contribute to a plateau in the intermediate scattering function. Our approach also disclosed a question about the influence on the properties of proton dynamics of secondary hydrogenated species.

#### 4.1.2 Paper II

In this paper, the dynamics of the very same samples as in Paper I were studied at shorter time scales, in the ps region, and within the more extended  $Q$ -range of *ca* 1.7–3.9 Å<sup>-1</sup>, at the IN5 TOF spectrometer. The aim of this experiment was to provide more insights into the microscopic mechanism of the local proton dynamics observable in this experimental window. In particular, extending the length scale towards higher  $Q$ -values in respect to a previous experiment with the same technique was suggested to be determinant to unambiguously discriminate between the spatial geometry related to the two fundamental steps of proton diffusion: i) proton transfers between neighbouring oxygens and ii) rotational motion of the -OH group, modelled respectively as a jump diffusion over 2 or 4 equivalent sites on a circle.

Our results show the presence of localised proton dynamics with onset between 200 K and 300 K upon increasing temperature and characterised by a quasi-elastic broadening in the energy range of *ca* 0.1-0.7 meV (full width at half maximum) between 300 K and 550 K. Interpreting these results within the

framework of the jump diffusion over 2 or 4 sites, the characteristic residence times are in a range of *ca* 4–30 ps for the transfers and *ca* 2–15 ps for rotations. The geometry of the dynamics is compatible with both the processes, with jump lengths or O-H distances that are well in line with values reported in literature from structural studies or local dynamics in similar materials. Further, the presence of a considerable fraction of immobile species is noticed, whose origin remains to be verified in future. We also observed low energy barriers, of the order of 100 meV, and small differences between the two systems, which cannot be correlated with the large differences in proton conductivity in these materials. These observations hint at the fact that the probed dynamics is not rate-limiting for long-range proton diffusion. By comparing the experimental results with those obtained from published DFT calculations, the hypothesis that the observed motion is an average description of many different dynamical processes, related to the presence of different proton sites, is suggested.



# Chapter 5

## Conclusions and outlook

Neutron scattering techniques, and in particular quasi-elastic neutron scattering, were applied to investigate the details of the proton dynamics in hydrated acceptor doped barium zirconates, which are well known proton conducting oxides. A comprehensive knowledge of the proton conduction mechanism, which may allow the design of new materials with high conductivities and chemical stability, is required to enable the use of important technological environmentally friendly devices, such as next generation intermediate- and low-temperature SOFCs.

The neutron spin echo investigation on hydrated  $\text{BaZr}_{0.9}\text{M}_{0.1}\text{O}_{2.95}$  ( $M = \text{Y}$  and  $\text{Sc}$ ) showed the presence of proton dynamics characterised by a stretched profile, most likely reflecting a wide distribution of local proton configurations, as suggested by infrared spectroscopy measurements. These dynamics appear more and more pronounced increasing the temperature, but strongly dependent neither on the  $Q$ -value, in the investigated range of  $0.69\text{--}1.23 \text{ \AA}^{-1}$ , nor on the dopant atom  $M$ . In the investigation of the local dynamics of the same samples with time-of-flight spectroscopy, it was observed a localised proton motion with low activation energy and no strong dependence on the dopant atom  $M$ . The

---

observed dynamics are compatible with both the transfer between two adjacent oxygens and the rotational motion of the -OH group, but also with an averaged of the contribution of several proton motions, related to the disordered nature of these materials. Both studies suggested the presence of immobile hydrogenated species, and our careful characterization of the hydration level by thermogravimetric analysis and polarized neutron diffraction disclosed the presence of an unexpectedly high hydrogen concentration. Different hydrogenated species can be hypothesised to contribute, and how they would affect the properties of the proton conduction remains to be investigated.

From an experimental point of view, the combination of many neutron scattering instruments, with different resolution and dynamical range appears crucial to get a comprehensive view over the proton conduction mechanism. The need of a thoroughly characterization of the samples is also clear, and in this respect important information about the hydrogen concentration were obtained in this study from polarised neutron diffraction measurements. The use of polarised neutrons in the investigation of proton conducting materials might be further extended to dynamical measurements, possibly representing a relevant improvement for future studies, for example allowing to explore the incoherent dynamics in those  $Q$ -ranges affected by the presence of the Bragg peaks and to clearly distinguish between collective motions and self-dynamics. Furthermore, it would be of high interest to investigate the behaviour of proton conducting oxides in conditions similar to those in a fuel cell under operation. In this respect, the progresses in technical devices allowing so are very interesting. For example, it has been developed a cell that permits QENS studies at high temperatures in a controlled vapour environment [93]. Such *in situ* studies may also contribute to a deeper understanding of the hydration process in these materials, which is not completely understood.

Finally, the additional insights into the proton conduction mechanism achieved

by comparing the experimental results with simulation data underline how the combination with computational studies might constitute an important support in the analysis and interpretation of the QENS data.

The results presented in this thesis are part of a more extended experimental study, yet in progress, of the proton dynamics in acceptor doped barium zirconates. The analysis of the experiments on In-doped barium zirconates with different doping level, for example, might help the understanding of the mechanistic details of the proton motions and of the influence of the doping level.



# Appendix A

## Hydration/dehydration equilibrium

### A.1 Concentration of protonic defects

To derive the theoretical concentration of protonic defects as a function of temperature, we start from Eq. 1.1, reported here again for convenience:



where  $V_{\text{O}}^{\bullet\bullet}$  is the oxygen vacancy,  $\text{O}_{\text{O}}^{\times}$  is the oxide ion, and  $\text{OH}_{\text{O}}^{\bullet}$  is the hydroxyl ion. Assuming an ideal behaviour of all the species involved, the equilibrium constant is given by [94]:

$$K = \frac{[\text{OH}_{\text{O}}^{\bullet}]^2}{[V_{\text{O}}^{\bullet\bullet}][\text{O}_{\text{O}}^{\times}]p_w}. \quad (\text{A.2})$$

The partial pressure of vapour  $p_w$  can be calculated using Dalton law, multiplying the molar fraction of vapour  $x_w$  with the total pressure  $p$ :  $p_w = x_w p$  [94]. If no ideal behaviour is assumed, activities and fugacity should be used instead of concentrations and pressure [94]. The temperature dependence of the equilibrium constant is given by [94]:

$$K = \exp\left(\frac{-\Delta G^0}{k_B T}\right), \quad (\text{A.3})$$

where  $\Delta G^0$  is the standard-state<sup>1</sup> Gibbs energy of the reaction and  $k_B$  is the Boltzmann constant. The site restriction gives:

$$N_O = [\text{OH}_O^\bullet] + [\text{V}_O^{\bullet\bullet}] + [\text{O}_O^\times], \quad (\text{A.4})$$

where  $N_O$  is the number of oxygen sites per formula unit, which is 3 for a perovskite. Assuming a single acceptor dopant  $M$ , and that only vacancies and protons compensate for the dopant, the charge neutrality condition gives:

$$0 = 2[\text{V}_O^{\bullet\bullet}] + [\text{OH}_O^\bullet] - [M]. \quad (\text{A.5})$$

We thus arrive to Eq. 1.2 [25], reported here again for convenience :

$$[\text{OH}_O^\bullet] = N_O \frac{K'}{K' - 4} \left[ 1 - \sqrt{1 - \frac{K' - 4}{K'} \left( \frac{2[M]}{N_O} - \frac{[M]^2}{N_O^2} \right)} \right], \quad (\text{A.6})$$

where  $K' = p_w K$ . The treatment can be further refined by considering the effective acceptor dopant concentration,  $S$  [61]. The equation 1.2 is therefore slightly modified and, with  $N_O = 3$ , becomes [61]:

$$[\text{OH}_O^\bullet] = \frac{3K' - \sqrt{K'(9K' - 6K'S + K'S^2 + 24S - 4S^2)}}{K' - 4} \quad (\text{A.7})$$

## A.2 Details of the calculation of the hydration curves

Hydration standard-state enthalpies  $\Delta H^0$  and entropies  $\Delta S^0$  were taken from Ref. [61], and used to calculate  $\Delta G^0 = \Delta H^0 - T\Delta S^0$  [94]. To approximate the conditions in the laboratory, a relative humidity (R.H.) value of 40%, a typical value of a quite dry indoor ambient, was chosen. The vapour partial pressure was derived from the relative humidity:

$$R.H. = \frac{p_w}{p_w^*}, \quad (\text{A.8})$$

---

<sup>1</sup>1 atm, 298.15 K

where  $p_w^*$  is the saturated vapour pressure, calculated using Clausius-Clapeyron equation [94]. The vapour partial pressure for hydration conditions was taken from Ref. [95].

For simulating the conditions in a tightly closed cell, it was considered to be sealed at ambient conditions ( $p= 1$  atm and temperature of 25 °C) and a relative humidity of 40%. Moistened air has been considered a perfect gas at these conditions. The total pressure in the cell during heating was calculated using van der Waals coefficients and second virial expansion, to take into account possible deviations from ideality at higher pressure [94]. Van der Waals coefficients were estimated considering a mixture of vapour and dry air (which was approximated by a composition of 80% N<sub>2</sub>, 20% O<sub>2</sub>), according to the calculated  $x_w$ . In a more rigorous treatment, vapour fugacity instead of vapour pressure could be used [94]. However, this was considered a sufficiently good approximation for our purpose.



# Appendix B

## Instrumentation and data treatment

### B.1 Time-of-flight spectroscopy

The instruments that apply the TOF method to record the energy transfer, after having selected an initial energy, are usually called *direct geometry TOF spectrometers* [83–85]. In these instruments, the incident beam needs to be pulsed and monochromatized. The monochromatization defines a precise wavelength of the neutron before the scattering event. However, neutrons in a continuous monochromatic incident beam would be indistinguishable. Pulsing the beam permits to label them: all the neutrons travelling in a monochromatic pulse have the same, well-defined, initial time. They differ in their arrival time to the detector bank, depending on whether they have lost, gained or conserved their energy during the scattering with the sample.

Some instruments make use of the TOF method to achieve a pulsed monochromatized incident beam, with a series of *disk choppers*: absorbing disks with transparent slits, rotating in the plane perpendicular to the beam direction

[83–85]. This is the case of the IN5 [87] spectrometer at ILL, whose scheme is depicted in Figure B.1. The beam is first pulsed by the two counter-rotating disks forming the pulsing chopper system (P). The contaminant chopper (CO) reduces the large bandwidth by removing harmonics, and the frame overlap chopper (FO) suppresses some of the produced pulses, in order to avoid that the slowest neutrons from a pulse overlap at the detector with the fastest neutrons from the next pulse. The monochromator choppers (M) are two counter-rotating disks that, being synchronized with the pulsing chopper, allow the passage of neutrons with only a desired wavelength, absorbing all the neutrons which travel faster or slower. The direct TOF instruments using this technology are usually called *disk chopper direct geometry TOF*, or also *TOF-TOF* spectrometers, since they use the TOF method twice: to pulse and monochromatize the incident beam and also to record the energy transfer [83–85]. The TOFTOF spectrometer at FRM II is another example of this kind of instruments, and it is very similar to IN5. One of the main differences, from the point of view of the users, is the detector. Both instruments use detectors based on  $^3\text{He}$  technology: TOFTOF has 1000 tubes covering about  $12\text{m}^2$ , whereas IN5 has 384 position sensitive tubes (PSD), covering about  $30\text{ m}^2$ . The use of PSD tubes allows a determination of  $\mathbf{Q}$ , thus IN5 can be exploited also for single crystals measurements.

In other direct geometry TOF instruments, like IN6 [87] at ILL, the incoming wavelength is selected by a single crystal monochromator, and the beam is then pulsed by a *Fermi chopper*, *i.e.* a collimator turning around an axis perpendicular to the beam direction. These instruments are sometimes called *direct geometry hybride TOF* [83–85].

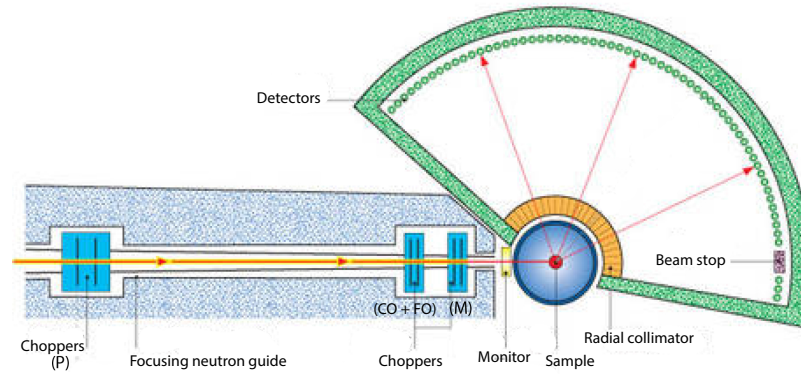


Figure B.1: Schematic representation of the IN5 TOF spectrometer at ILL, taken and modified from Ref. [87].

### B.1.1 TOF data treatment

Normally, for a QENS experiment on TOF instruments, measurements of at least the sample in its sample holder, an empty cell and a vanadium standard are required. A typical data reduction can be summarised as follows:

1. The raw data are normalised to monitor or counting time. The monitor normalisation is usually preferred since it takes into account possible fluctuations of the incoming flux.
2. The measurement of the empty holder, weighted for the transmission factor of the sample, is subtracted from the measurements of the sample in its sample holder.
3. The efficiency and solid angle coverage of the different detectors are corrected using a vanadium standard, which is approximatively considered as a purely incoherent scatterer. The vanadium spectra are integrated over the channels of the elastic peak. This integral is used to divide the sample data. The intensity decrease of the scattering of the vanadium due to the

Debye-Waller factor is taken into account. In this step, a relative (and possibly absolute) normalisation of the spectra is also achieved.

4. Spectra from blind or noisy detectors are removed.
5. A flat additional background, if present, is subtracted. This step is particularly important if the subtraction of the empty can is not available.
6. The energy dependence of the detector efficiency is corrected. Since many factors need to be taken into account the exact calculation is not trivial, and an empirical function is normally used [85].
7. The intensities recorded as a function of TOF and the position on the detector, the latter identifying the scattering angle, are converted into the energy and momentum space.

Further corrections may consider the effect of multiple scattering and of the absorption and self-shielding of the sample. Finally, we note that since the instrumental resolution is convoluted with the dynamic structure factor, during the fitting procedure of the spectra a convolution is usually required. Therefore, an equidistant energy binning could be needed.

## B.2 Backscattering spectroscopy

The importance of the backscattering condition to achieve a high resolution appears clear differentiating the Bragg-condition,  $\lambda = 2d\sin\vartheta$ , where  $\lambda$  is the wavelength,  $d$  is the lattice parameter and  $2\vartheta$  is the angle between the incoming and reflected beam. We obtain

$$\frac{\Delta\lambda}{\lambda} = \frac{\Delta d}{d} + \Delta\vartheta\cot\vartheta, \quad (\text{B.1})$$

and we can therefore notice that the reflected wavelength band  $\Delta\lambda$  becomes minimal for  $\vartheta = 90^\circ$ . Moreover, in the backscattering condition, the width of

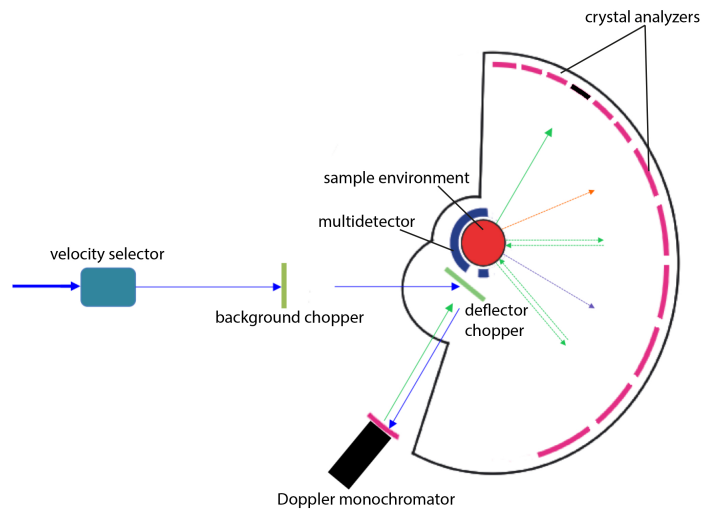


Figure B.2: Schematic representation of the IN16b backscattering spectrometer at ILL, redrawn from Ref. [96].

the reflected wavelength band is independent, in this first order approximation, from the beam divergence  $\Delta\vartheta$ , and only depends on the term  $\Delta d/d$ , which is related to the quality of the crystal [86].

Figure B.2 shows a scheme of the neutron backscattering spectrometer IN16b [87] at ILL, illustrated in its “high flux” configuration. The incident wavelength band is selected by a velocity selector. The background chopper pulses the beam, and a rotating deflector sends the beam to the monochromator, where the energy is selected with high precision. Due to the pulsed structure of the beam, the neutrons reflected by the monochromator are allowed to pass back through an open window in the rotating deflector and reach the sample, by which they are scattered in all directions. Only those neutrons having a certain final energy, determined by the backscattering reflection at the analyser crystals, are reflected to the detectors and counted.

The monochromator is mounted on a Doppler device that allows to move it backwards and forwards with different velocities. The energy of the neutrons

after reflection from a moving monochromator is  $E_i + \Delta E$ , where  $E_i$  is the neutron energy that would be reflected by the monochromator at rest and  $\Delta E$  is

$$\Delta E = 2 \frac{v_D}{v} E_i, \quad (\text{B.2})$$

where  $v$  is the neutron velocity and  $v_D$  the Doppler velocity. This is valid in a first order approximation for  $v_D \ll v$  [86]. Depending on if and how the Doppler is moving, different types of measurements can be done:

- Elastic fixed window scan (EFWS): the monochromator is resting, and all the neutrons reaching the detector have therefore been scattered elastically (within the instrumental resolution) by the sample. The elastic intensity can be recorded as a function of sample temperature, giving an overview of the dynamics in the sample. In fact, when dynamical processes under the effect of the increasing temperature become faster than the time defined by the energy resolution, the observed intensity decreases. An extension of this mode is the inelastic fixed window scan (IFWS) [97], currently available only at IN16b. During this scan the goal is to measure as long as possible at a chosen energy transfer, *i.e.* at a constant Doppler velocity. While the sample temperature continuously increases, different inelastic energy transfer windows can be cycled. The advantage of the fixed window scans is that the temperature dependence can be quickly obtained with good statistics.
- Energy transfer spectra: a full energy transfer spectrum at fixed temperature can be obtained periodically modulating the incident energy, by moving the Doppler monochromator with a sinusoidal velocity profile. The neutron counts from the detectors are sorted into a spectrum as a function of the energy transfer by a multichannel analyser. The energy transfer

range is typically limited to a few tens/hundreds of  $\mu\text{eV}$  [87, 88].

### B.2.1 BS data treatment

Data reduction for backscattering QENS spectra starts with the first three points already explained for the TOF measurements. The data are then transformed from energy channels to energy transfer, and the angles are translated into  $Q$ -values. The small probed energy transfer interval allows to neglect the energy dependence of  $Q$ . Corrections for attenuation and multiple scattering may be applied in addition.

## B.3 Neutron spin-echo spectroscopy

As introduced in 3.3, in neutron spin-echo the velocity change of incident and scattered neutrons are measured using the Larmor precession of the neutron spin in an external magnetic field [89–91]. A polarised neutron beam enters in a magnetic field region and subsequently into another with the same length and a magnetic field of the same strength but opposite direction. At the quasielastic limit, where the energy transfers are small compared with the incoming energy, the total precession angle,  $\phi$ , is directly proportional to the energy transfer and the NSE Fourier time  $t$ , which can be written as:

$$t = \frac{\hbar\gamma}{m_n v^3} \int B dl, \quad (\text{B.3})$$

where  $\gamma$  is the gyromagnetic ratio of the neutron,  $m_n$  is the neutron mass,  $v$  is the neutron velocity,  $\hbar$  is the reduced Planck constant, and  $\int B dl$  is the field integral, *i.e.* the integral of the external magnetic field  $B$  along the neutron trajectory. The quasi-elastic condition is fulfilled for the whole dynamic range covered in a NSE experiment. The measured polarization in NSE is thus:

$$P = \langle \cos \phi \rangle = \frac{\int \cos(\omega t) S(Q, \omega) d\omega}{\int S(Q, \omega) d\omega}. \quad (\text{B.4})$$

In a NSE experiment we therefore directly obtain the real part of the normalised intermediate scattering function. As a result, the instrumental resolution, that is convoluted with the dynamic structure factor in an experiment in the  $(Q, \omega)$  phase space, is here simply multiplied. The signal from a totally elastic scatterer is therefore measured and used to divide the signal from the data [89, 90].

The use of polarised neutrons allows the estimation of the nuclear and spin-incoherent scattering relative weights. In the materials of our interest, they can very well approximate, respectively, the coherent and incoherent scattering relative weights, here indicated as  $I_{\text{coh}}(Q, t = 0) = S_{\text{coh}}(Q)$  and  $I_{\text{inc}}(Q, t = 0) = S_{\text{inc}}(Q)$ . The normalised intermediate scattering function can be hence written as [89]:

$$\frac{I(Q, t)_{\text{NSE}}}{I(Q, t = 0)_{\text{NSE}}} = \frac{I_{\text{coh}}(Q, t) - \frac{1}{3}I_{\text{inc}}(Q, t)}{S_{\text{coh}}(Q) - \frac{1}{3}S_{\text{inc}}(Q)}, \quad (\text{B.5})$$

From Eq. B.5, we note that if one of the components shows no dynamics, the complete decay of the NSE intermediate scattering takes values that depend on the the relative weights of coherent and incoherent scattering, *i.e.* on the sample composition, and these values can be also negative. This has to be taken into account to compare the NSE data from different samples, with different coherent/incoherent ratios, but also with the  $I(Q, t)$  that can be derived, for example, by Fourier transforming the dynamic structure factor obtained with a TOF or BS spectrometer. In the case of our measurements on hydrated Y- and Sc-doped barium zirconates at the IN11 [87] spectrometer at ILL, considerations on the different contributions and an accurate evaluation of the hydrogen concentration in the materials allowed us to calculate the level of an hypothetical complete decay of the  $I(Q, t)$  within the experimental time window. This is described in detail in Paper I.

The different effect on the polarization of the coherent and incoherent contributions has other important consequences in the application of neutron spin-

echo on proton conductors. These systems are prevalently incoherent scatterers, and the  $-1/3$  factor in polarization decreases the statistical accuracy. As mentioned in 2.1, the coherent scattering intensity changes strongly with  $Q$ . If at some  $Q$ -values the incoherent contribution is about three times higher than the coherent one, the resulting polarization will be zero at those values, making the measurement difficult. A multidetector option helps to compensate for the low intensity. It also permits to have a quick overview of the coherent/incoherent ratios over a wide range of  $Q$ -values and therefore to possibly select the best region for the measurement. This option was used during our experiment described in Paper I, for which we exploited the  $30^\circ$  wide-angle detector of the IN11-C setup [87, 89], shown in Figure B.3.

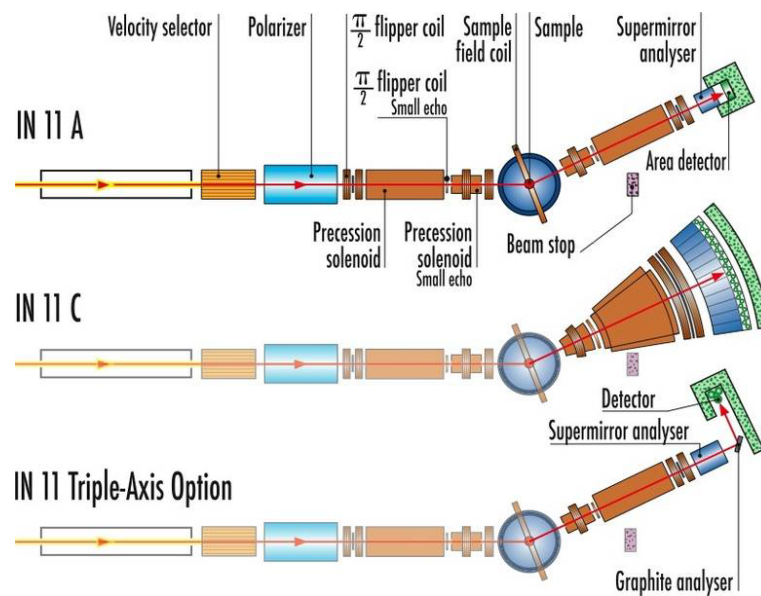


Figure B.3: Schematic representation of the IN11 NSE spectrometer at ILL, taken from Ref. [87].

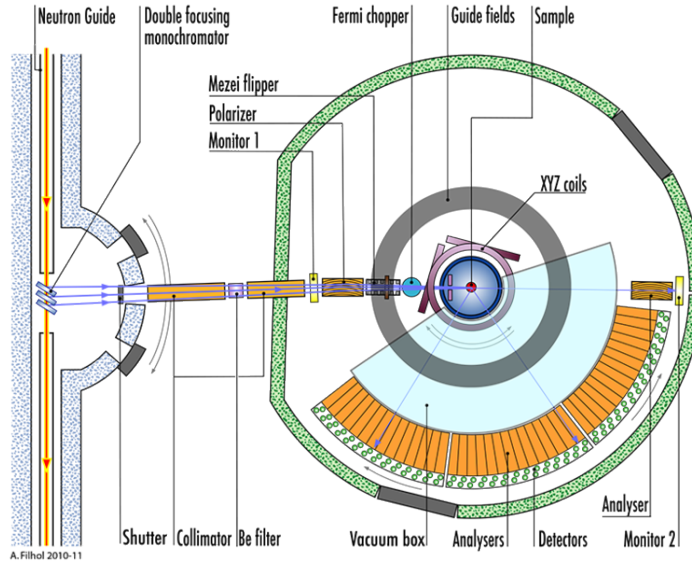


Figure B.4: Schematic representation of the diffuse scattering spectrometer D7 at ILL, taken from Ref. [87].

## B.4 Polarization analysis at D7

The scheme of the diffuse scattering spectrometer D7 [79,87] at ILL is presented in Figure B.4. The incident wavelength (3.1, 4.8 or 5.8 Å) is selected by the monochromator, and the beam is polarised in the  $z$ -direction. The neutrons then pass through a Mezei spin-flipper, which is "off" when measuring non-spin-flip cross-sections, and "on" when measuring spin-flip cross-sections. The polarization of neutrons is set into the  $x$ -,  $y$ - or  $z$ -direction using three orthogonal magnetic coils situated at the sample position. After being scattered from the sample, the neutrons are analysed for final spin state, and detected using the three multi-analyser/detector banks.

In addition to usual data corrections, such as background contribution and detector efficiency, the polarization analysis requires corrections for the finite polarization of the incident beam and for the analysing power of the analysers

in the scattered beam. A quartz sample is commonly used for this purpose. A vanadium standard of known mass provides an absolute normalisation of the measured cross section [79].



# Bibliography

- [1] E. D. Wachsman and K. T. Lee, “Lowering the temperature of solid oxide fuel cells,” *Science (New York, N.Y.)*, vol. 334, pp. 935–9, nov 2011.
- [2] E. Wachsman, T. Ishihara, and J. Kilner, “Low-temperature solid-oxide fuel cells,” *MRS Bulletin*, vol. 39, pp. 773–779, sep 2014.
- [3] N. Q. Minh, “Solid oxide fuel cell technology-features and applications,” *Solid State Ionics*, vol. 174, pp. 271–277, oct 2004.
- [4] L. Carrette, K. A. Friedrich, and U. Stimming, “Fuel Cells: Principles, Types, Fuels, and Applications,” *ChemPhysChem*, vol. 1, no. 4, pp. 162–193, 2000.
- [5] D. J. L. Brett, A. Atkinson, N. P. Brandon, and S. J. Skinner, “Intermediate temperature solid oxide fuel cells,” *Chemical Society Reviews*, vol. 37, pp. 1568–78, aug 2008.
- [6] M. Karlsson, “Perspectives of neutron scattering on proton conducting oxides,” *Dalton Transactions*, vol. 42, pp. 317–29, jan 2013.
- [7] K.-D. Kreuer, “Proton-Conducting Oxides,” *Annual Review of Materials Research*, vol. 33, pp. 333–359, aug 2003.

## BIBLIOGRAPHY

---

- [8] M. Karlsson, “Proton dynamics in oxides: insight into the mechanics of proton conduction from quasielastic neutron scattering,” *Physical Chemistry Chemical Physics*, vol. 17, no. 1, pp. 26–38, 2015.
- [9] R. Hempelmann, *Quasielastic Neutron Scattering and Solid State Diffusion*. Oxford University Press, nov 2000.
- [10] K.-D. Kreuer, “Proton conductivity: materials and applications,” *Chemistry of Materials*, no. 19, pp. 610–641, 1996.
- [11] L. Malavasi, C. A. J. Fisher, and M. S. Islam, “Oxide-ion and proton conducting electrolyte materials for clean energy applications: structural and mechanistic features,” *Chemical Society Reviews*, vol. 39, pp. 4370–87, nov 2010.
- [12] T. Ishihara, ed., *Perovskite Oxide for Solid Oxide Fuel Cells*. Fuel Cells and Hydrogen Energy, Boston, MA: Springer US, 2009.
- [13] E. Fabbri, D. Pergolesi, and E. Traversa, “Materials challenges toward proton-conducting oxide fuel cells: a critical review,” *Chemical Society reviews*, vol. 39, no. 11, pp. 4355–4369, 2010.
- [14] T. Norby, “Proton conduction in Ca- and Sr-substituted LaPO<sub>4</sub>,” *Solid State Ionics*, vol. 77, pp. 240–243, apr 1995.
- [15] Y. Larring, “Protons in rare earth oxides,” *Solid State Ionics*, vol. 77, pp. 147–151, apr 1995.
- [16] R. Haugsrud and T. Norby, “Proton conduction in rare-earth ortho-niobates and ortho-tantalates,” *Nature Materials*, vol. 5, pp. 193–196, feb 2006.
- [17] R. Hui, R. Maric, C. Decès-Petit, E. Styles, W. Qu, X. Zhang, J. Roller, S. Yick, D. Ghosh, K. Sakata, and M. Kenji, “Proton conduction in ceria-

- doped  $\text{Ba}_2\text{In}_2\text{O}_5$  nanocrystalline ceramic at low temperature,” *Journal of Power Sources*, vol. 161, pp. 40–46, oct 2006.
- [18] T. Shimura, M. Komori, and H. Iwahara, “Ionic conduction in pyrochlore-type oxides containing rare earth elements at high temperature,” *Solid State Ionics*, vol. 86-88, pp. 685–689, jul 1996.
- [19] T. Takahashi and H. Iwahara, “Solid-State Ionics - Protonic Conduction in Perovskite Type Oxide Solid-Solutions,” *Revue De Chimie Minerale*, vol. 17, no. 4, pp. 243–253, 1980.
- [20] E. Fabbri, A. Magrasó, and D. Pergolesi, “Low-temperature solid-oxide fuel cells based on proton-conducting electrolytes,” *MRS Bulletin*, vol. 39, pp. 792–797, sep 2014.
- [21] B. C. Steele and A. Heinzl, “Materials for fuel-cell technologies,” *Nature*, vol. 414, pp. 345–52, nov 2001.
- [22] M. De Graef and M. E. McHenry, *Structure of Materials An Introduction to Crystallography, Diffraction and Symmetry*. Cambridge: Cambridge University Press, 1st ed., 2007.
- [23] V. M. Goldschmidt, “Die Gesetze der Krystallochemie,” *Naturwissenschaften*, vol. 14, no. 21, pp. 477–485, 1926.
- [24] P. Davies, H. Wu, A. Borisevich, I. Molodetsky, and L. Farber, “Crystal Chemistry of Complex Perovskites: New Cation-Ordered Dielectric Oxides,” *Annual Review of Materials Research*, vol. 38, pp. 369–401, aug 2008.
- [25] J. B. Nyman, E. E. Helgee, and G. Wahnström, “Oxygen vacancy segregation and space-charge effects in grain boundaries of dry and hydrated  $\text{BaZrO}_3$ ,” *Applied Physics Letters*, vol. 100, p. 061903, feb 2012.

## BIBLIOGRAPHY

---

- [26] H. Iwahara, H. Uchida, and N. Maeda, "High temperature fuel and steam electrolysis cells using proton conductive solid electrolytes," *Journal of Power Sources*, vol. 7, pp. 293–301, jan 1982.
- [27] T. Norby and Y. Larring, "Concentration and transport of protons in oxides," *Current Opinion in Solid State and Materials Science*, vol. 2, pp. 593–599, oct 1997.
- [28] C. J. T. de Grotthuss, "Sur la décomposition de l'eau et des corps qu'elle tient en dissolution à l'aide de l'électricité galvanique," *Ann. Chim. (Paris)*, vol. 58, no. 1806, pp. 54–74, 1806.
- [29] W. Münch, G. Seifert, K.-D. Kreuer, and J. Maier, "A quantum molecular dynamics study of proton conduction phenomena in BaCeO<sub>3</sub>," *Solid State Ionics*, vol. 86-88, pp. 647–652, jul 1996.
- [30] W. Münch, G. Seifert, K.-D. Kreuer, and J. Maier, "A quantum molecular dynamics study of the cubic phase of BaTiO<sub>3</sub> and BaZrO<sub>3</sub>," *Solid State Ionics*, vol. 97, pp. 39–44, may 1997.
- [31] M. Pionke, T. Mono, W. Schweika, T. Springer, and H. Schober, "Investigation of the hydrogen mobility in a mixed perovskite: Ba[Ca<sub>(1+x)/3</sub>Nb<sub>(2-x)/3</sub>]O<sub>3-x/2</sub> by quasielastic neutron scattering," *Solid State Ionics*, vol. 97, pp. 497–504, may 1997.
- [32] D. Wilmer, T. Seydel, and K.-D. Kreuer, "Proton Diffusion in Hydrated Acceptor-Doped Barium Zirconate," *MRS Proceedings*, vol. 972, pp. 0972–AA01–04, jan 2006.
- [33] R. Hempelmann, M. Soetratmo, O. Hartmann, and R. Wäppling, "Muon diffusion and trapping in proton conducting oxides," *Solid State Ionics*, vol. 107, pp. 269–280, apr 1998.

- [34] M. Karlsson, A. Matic, E. Zanghellini, and I. Ahmed, “Temperature-Dependent Infrared Spectroscopy of Proton-Conducting Hydrated Perovskite  $\text{BaIn}_x\text{Zr}_{1-x}\text{O}_{3-x/2}$  ( $x=0.10-0.75$ ),” *The Journal of Physical Chemistry C*, vol. 114, pp. 6177–6181, apr 2010.
- [35] M. Karlsson, M. E. Björketun, P. Sundell, A. Matic, G. Wahnström, D. Engberg, L. Börjesson, I. Ahmed, S.-G. Eriksson, and P. Berastegui, “Vibrational properties of protons in hydrated  $\text{BaIn}_x\text{Zr}_{1-x}\text{O}_{3-x/2}$ ,” *Physical Review B*, vol. 72, p. 094303, sep 2005.
- [36] K.-D. Kreuer, “Aspects of the formation and mobility of protonic charge carriers and the stability of perovskite-type oxides,” *Solid State Ionics*, vol. 125, pp. 285–302, oct 1999.
- [37] M. E. Björketun, P. Sundell, and G. Wahnström, “Effect of acceptor dopants on the proton mobility in  $\text{BaZrO}_3$ : A density functional investigation,” *Physical Review B*, vol. 76, p. 054307, aug 2007.
- [38] D.-H. Kim, B.-K. Kim, and Y.-C. Kim, “Energy barriers for proton migration in yttrium-doped barium zirconate super cell with  $\Sigma 5$  (310)/[001] tilt grain boundary,” *Solid State Ionics*, vol. 213, pp. 18–21, 2012.
- [39] M. A. Gomez, M. A. Griffin, S. Jindal, K. D. Rule, and V. R. Cooper, “The effect of octahedral tilting on proton binding sites and transition states in pseudo-cubic perovskite oxides,” *The Journal of Chemical Physics*, vol. 123, no. 9, p. 094703, 2005.
- [40] Q. Zhang, G. Wahnström, M. E. Björketun, S. Gao, and E. Wang, “Path integral treatment of proton transport processes in  $\text{BaZrO}_3$ ,” *Physical Review Letters*, vol. 101, no. November, pp. 1–4, 2008.

- [41] P. Raiteri, J. D. Gale, and G. Bussi, "Reactive force field simulation of proton diffusion in BaZrO<sub>3</sub> using an empirical valence bond approach," *Journal of Physics. Condensed matter : an Institute of Physics journal*, vol. 23, p. 334213, aug 2011.
- [42] B. Groß, C. Beck, F. Meyer, T. Krajewski, R. Hempelmann, and H. Altgeld, "BaZr<sub>0.85</sub>Me<sub>0.15</sub>O<sub>2.925</sub> (Me=Y, In and Ga): crystal growth, high-resolution transmission electron microscopy, high-temperature X-ray diffraction and neutron scattering experiments," *Solid State Ionics*, vol. 145, pp. 325–331, dec 2001.
- [43] C. Beck, S. Janssen, B. Groß, and R. Hempelmann, "Neutron time-of-flight spectrometer FOCUS at SINQ: results from nanocrystalline matter studies," *Scripta Materialia*, vol. 44, pp. 2309–2313, may 2001.
- [44] A. K. Azad, C. Savaniu, S. Tao, S. Duval, P. Holtappels, R. M. Ibberson, and J. T. S. Irvine, "Structural origins of the differing grain conductivity values in BaZr<sub>0.9</sub>Y<sub>0.1</sub>O<sub>2.95</sub> and indication of novel approach to counter defect association," *Journal of Materials Chemistry*, vol. 18, p. 3414, jul 2008.
- [45] P. Colomban, O. Zaafrani, and A. Slodczyk, "Proton content and nature in perovskite ceramic membranes for medium temperature fuel cells and electrolyzers," *Membranes*, vol. 2, pp. 493–509, jan 2012.
- [46] N. Jalarvo, L. Stingaciu, D. Gout, Z. Bi, M. P. Paranthaman, and M. Ohl, "Proton dynamics in La<sub>0.8</sub>Ba<sub>1.2</sub>GaO<sub>3.9</sub> · nH<sub>2</sub>O studied by quasielastic incoherent neutron scattering," *Solid State Ionics*, vol. 252, pp. 12–18, dec 2013.
- [47] T. Norby, M. Wideroe, R. Glockner, and Y. Larring, "Hydrogen in oxides," *Dalton Transactions*, pp. 3012–8, oct 2004.

- 
- [48] M. S. Islam, R. A. Davies, and J. D. Gale, "Proton Migration and Defect Interactions in the  $\text{CaZrO}_3$  Orthorhombic Perovskite: A Quantum Mechanical Study," *Chemistry of Materials*, vol. 13, pp. 2049–2055, may 2001.
- [49] M. Gomez, M. Chundururu, L. Chigweshe, L. Foster, S. J. Fensin, K. M. Fletcher, and L. E. Fernandez, "The effect of yttrium dopant on the proton conduction pathways of  $\text{BaZrO}_3$ , a cubic perovskite," *The Journal of Chemical Physics*, vol. 132, p. 214709, jun 2010.
- [50] M. S. Islam, R. A. Davies, and J. D. Gale, "Hop, skip or jump? Proton transport in the  $\text{CaZrO}_3$  perovskite oxide," *Chemical Communications*, vol. 3, no. 7, pp. 661–662, 2001.
- [51] Q. Chen, J. Banyte, X. Zhang, J. P. Embs, and A. Braun, "Proton diffusivity in spark plasma sintered  $\text{BaCe}_{0.8}\text{Y}_{0.2}\text{O}_{3-\delta}$ : In-situ combination of quasi-elastic neutron scattering and impedance spectroscopy," *Solid State Ionics*, vol. 252, pp. 2–6, dec 2013.
- [52] R. Hempelmann, C. Karmonik, T. Matzke, M. Cappadonia, U. Stimming, T. Springer, and M. A. Adams, "Quasielastic neutron scattering study of proton diffusion in  $\text{SrCe}_{0.95}\text{Yb}_{0.05}\text{H}_{0.02}\text{O}_{2.985}$ ," *Solid State Ionics*, vol. 77, no. 94, pp. 152–156, 1995.
- [53] T. Matzke, U. Stimming, C. Karmonik, M. Soetratmo, R. Hempelmann, and F. Guthoff, "Quasielastic thermal neutron scattering experiment on the proton conductor  $\text{SrCe}_{0.95}\text{Yb}_{0.05}\text{H}_{0.02}\text{O}_{2.985}$ ," *Solid State Ionics*, vol. 88, no. 96, pp. 621–628, 1996.
- [54] C. Karmonik, R. Hempeimann, J. Cook, F. Güthoff, U. Saarländes, and L. Langevin, "Investigation of the Proton Migration Mechanism in the Perovskite Proton Conductor  $\text{Ba}_3\text{Ca}_{1.18}\text{Nb}_{1.822}\text{H}_{0.2}\text{O}_{8.83}$  by means of Quasielastic Neutron Scattering," *Ionics*, vol. 2, pp. 69–74, 1996.

- [55] A. Braun, S. Duval, P. Ried, and J. Embs, “Proton Diffusivity in the  $\text{BaZr}_{0.9}\text{Y}_{0.1}\text{O}_{3-\delta}$  Proton Conductor,” *Journal of Applied Electrochemistry*, vol. 39, no. 4, pp. 471–475, 2009.
- [56] Y. Yamazaki, F. Blanc, Y. Okuyama, L. Buannic, J. C. Lucio-Vega, C. P. Grey, and S. M. Haile, “Proton trapping in yttrium-doped barium zirconate,” *Nature materials*, vol. 12, pp. 647–651, may 2013.
- [57] M. E. Björketun, P. Sundell, G. Wahnström, and D. Engberg, “A kinetic Monte Carlo study of proton diffusion in disordered perovskite structured lattices based on first-principles calculations,” *Solid State Ionics*, vol. 176, pp. 3035–3040, dec 2005.
- [58] P. G. Sundell, M. E. Björketun, and G. Wahnström, “Density-functional calculations of prefactors and activation energies for H diffusion in  $\text{BaZrO}_3$ ,” *Physical Review B*, vol. 76, no. 9, p. 094301, 2007.
- [59] M. S. Islam, P. R. Slater, J. R. Tolchard, and T. Dinges, “Doping and defect association in  $\text{AZrO}_3$  ( $A = \text{Ca}, \text{Ba}$ ) and  $\text{LaMO}_3$  ( $M = \text{Sc}, \text{Ga}$ ) perovskite-type ionic conductors.,” *Dalton Transactions*, vol. 3, pp. 3061–6, oct 2004.
- [60] N. Kitamura, J. Akola, S. Kohara, K. Fujimoto, and Y. Idemoto, “Proton Distribution and Dynamics in Y and Zn Doped  $\text{BaZrO}_3$ ,” *The Journal of Physical Chemistry C*, vol. 118, p. 140725075203008, 2014.
- [61] K.-D. Kreuer, S. Adams, W. Münch, A. Fuchs, U. Klock, and J. Maier, “Proton conducting alkaline earth zirconates and titanates for high drain electrochemical applications,” *Solid State Ionics*, vol. 145, pp. 295–306, dec 2001.
- [62] K.-D. Kreuer, “On the development of proton conducting materials for technological applications,” *Solid State Ionics*, vol. 97, pp. 1–15, may 1997.

- [63] D. Zeudmi Sahraoui and T. Mineva, “Effect of dopant nature on structures and lattice dynamics of proton-conducting  $\text{BaZrO}_3$ ,” *Solid State Ionics*, vol. 253, pp. 195–200, dec 2013.
- [64] F. Giannici, A. Longo, A. Balerna, K.-D. Kreuer, and A. Martorana, “Indium Doping in Barium Cerate: the Relation between Local Symmetry and the Formation and Mobility of Protonic Defects,” *Chemistry of Materials*, vol. 19, pp. 5714–5720, nov 2007.
- [65] M. Karlsson, A. Matic, D. Engberg, M. E. Björketun, M. M. Koza, I. Ahmed, G. Wahnström, L. Börjesson, and S.-G. Eriksson, “Quasielastic neutron scattering of hydrated  $\text{BaZr}_{0.90}\text{A}_{0.10}\text{O}_{2.95}$  ( $A=\text{Y}$  and  $\text{Sc}$ ),” *Solid State Ionics*, vol. 180, pp. 22–28, feb 2009.
- [66] M. Karlsson, P. Fouquet, I. Ahmed, and M. Maccarini, “Dopant Concentration and Short-Range Structure Dependence of Diffusional Proton Dynamics in Hydrated  $\text{BaIn}_x\text{Zr}_{1-x}\text{O}_{3-x/2}$  ( $x = 0.10$  and  $0.50$ ),” *The Journal of Physical Chemistry C*, vol. 114, pp. 3292–3296, feb 2010.
- [67] M. Karlsson, I. Ahmed, A. Matic, and S.-G. Eriksson, “Short-range structure of proton-conducting  $\text{BaM}_{0.10}\text{Zr}_{0.90}\text{O}_{2.95}$  ( $M=\text{Y}$ ,  $\text{In}$ ,  $\text{Sc}$  and  $\text{Ga}$ ) investigated with vibrational spectroscopy,” *Solid State Ionics*, vol. 181, pp. 126–129, feb 2010.
- [68] M. Karlsson, A. Matic, C. S. Knee, I. Ahmed, S.-G. Eriksson, and L. Börjesson, “Short-Range Structure of Proton-Conducting Perovskite  $\text{BaIn}_x\text{Zr}_{1-x}\text{O}_{(3-x/2)}$  ( $x = 0-0.75$ ),” *Chemistry of Materials*, vol. 20, pp. 3480–3486, may 2008.
- [69] M. Karlsson, A. Matic, S. F. Parker, I. Ahmed, L. Börjesson, and S. Eriksson, “O-H wag vibrations in hydrated  $\text{BaIn}_x\text{Zr}_{1-x}\text{O}_{3-x/2}$  investigated with

## BIBLIOGRAPHY

---

- inelastic neutron scattering,” *Physical Review B*, vol. 77, no. 10, p. 104302, 2008.
- [70] S. Lovesey, *Theory of neutron scattering from condensed matter*. London: Oxford University Press, 1984.
- [71] G. L. Squires, *Introduction to the Theory of Thermal Neutron Scattering*. Courier Corporation, 1978.
- [72] H. Schober, “Diffusion des neutrons par la matière cristalline ou amorphe non-magnétique,” *École thématique de la Société Française de la Neutronique*, vol. 10, pp. 159–336, 2010.
- [73] A. Messiah, *Quantum mechanics, volume I*. Amsterdam, The Netherlands: North-Holland Publishing Company, 1967.
- [74] L. van Hove, “Correlations in space and time and Born approximation scattering in systems of interacting particles,” *Physical Review*, vol. 95, no. 1, pp. 249–262, 1954.
- [75] V. F. Sears, “Neutron scattering lengths and cross sections,” *Neutron News*, vol. 3, no. 3, pp. 26–37, 1992.
- [76] R. M. Moon, T. Riste, and W. Koehler, “Polarization analysis of thermal-neutron scattering,” *Physical Review*, vol. 181, no. 2, pp. 920–931, 1969.
- [77] P. Gerlach, O. Schärpf, W. Prandl, and B. Dorner, “Separation of the coherent and incoherent scattering of  $C_2Cl_6$  by polarization analysis,” *Journal de Physique*, vol. 43, no. 12, pp. C7–151, 1982.
- [78] O. Schärpf and H. Capellmann, “TheXYZ-Difference Method with Polarized Neutrons and the Separation of Coherent, Spin Incoherent, and Magnetic Scattering Cross Sections in a Multidetector,” *Physica Status Solidi (a)*, vol. 135, pp. 359–379, feb 1993.

- [79] J. R. Stewart, P. P. Deen, K. H. Andersen, H. Schober, J.-F. Barthélémy, J. M. Hillier, a. P. Murani, T. Hayes, and B. Lindenau, “Disordered materials studied using neutron polarization analysis on the multi-detector spectrometer, D7,” *Journal of Applied Crystallography*, vol. 42, pp. 69–84, dec 2008.
- [80] M. Bée, *Quasielastic Neutron Scattering: principles and applications in solid state chemistry, biology and materials science*. Bristol and Philadelphia: Adam Hilger, 1988.
- [81] S. Yip, “Quasi-elastic scattering in neutron and laser spectroscopy,” in *Spectroscopy in biology and chemistry: neutrons, Xray, laser* (S.-H. Chen and S. Yip, eds.), Academic Press, 1974.
- [82] S. Peggs, R. Kreier, C. Carlile, ..., and J. Yeck, eds., *ESS Technical Design Report*. 2013.
- [83] H. Schober, “Neutron Scattering Instrumentation,” in *Neutron Applications in Earth, Energy and Environmental Sciences* (L. Liang, R. Rinaldi, and H. Schober, eds.), pp. 37–104, Boston, MA: Springer US, 2009.
- [84] T. Brückel, G. Heger, R. Zorn, and D. Richter, *Neutron Scattering : Lectures of the JCMS Laboratory Course held at Forschungszentrum Jülich and the research reactor FRM II of TU Munich ; In cooperation with RWTH Aachen and University of Münster*. Forschungszentrum, Zentralbibliothek, 2008.
- [85] J. Ollivier and J.-M. Zanotti, “Diffusion inélastique de neutrons par temps de vol,” *JDN 16 - Diffusion Inélastique des Neutrons pour l’Etude des Excitations dans la Matière Condensée*, vol. 10, pp. 379–423, 2010.
- [86] B. Frick, “Neutron Backscattering Spectroscopy,” in *Neutron and X-ray Spectroscopy*, pp. 483–527, Berlin/Heidelberg: Springer-Verlag, 2006.

- [87] “<http://www.ill.eu>.”
- [88] “<https://neutrons.ornl.gov/basis>.”
- [89] B. Farago, “The basics of Neutron Spin Echo,” in *Neutron Data Booklet* (A.-J. Dianoux and G. Lander, eds.), OCP Science, second edi ed., 2003.
- [90] F. Mezei, C. Pappas, and T. Gutberlet, eds., *Neutron Spin Echo Spectroscopy*, vol. 601 of *Lecture Notes in Physics*. Berlin, Heidelberg: Springer Berlin Heidelberg, dec 2003.
- [91] F. Mezei, “Neutron spin echo: A new concept in polarized thermal neutron techniques,” *Zeitschrift für Physik*, vol. 255, pp. 146–160, apr 1972.
- [92] M. Karlsson, D. Engberg, M. E. Björketun, A. Matic, G. Wahnström, P. G. Sundell, P. Berastegui, I. Ahmed, P. Falus, B. Farago, L. Börjesson, and S.-G. Eriksson, “Using Neutron Spin-Echo To Investigate Proton Dynamics in Proton-Conducting Perovskites,” *Chemistry of Materials*, vol. 22, pp. 740–742, feb 2010.
- [93] A. Al-Wahish, D. Armitage, U. Al-Binni, B. Hill, R. Mills, N. Jalarvo, L. Santodonato, K. W. Herwing, and D. Mandrus, “A new apparatus design for high temperature (up to 950 °C) quasi-elastic neutron scattering in a controlled gaseous environment,” *Review of Scientific Instruments*, no. 86, p. 095102, 2015.
- [94] D. A. Mc Quarrie and J. D. Simon, *Physical Chemistry. A molecular approach*. Sausalito: University Science Books, 1997.
- [95] I. Ahmed, F. G. Kinyanjui, S. M. H. Rahman, P. Steegstra, S. G. Eriksson, and E. Ahlberg, “Proton Conductivity in Mixed B-Site Doped Perovskite Oxide  $\text{BaZr}_{0.5}\text{In}_{0.25}\text{Yb}_{0.25}\text{O}_{3-\delta}$ ,” *Journal of The Electrochemical Society*, vol. 157, p. B1819, dec 2010.

- [96] M. A. Appel, “Ring Rotation in Ferrocene and Ferrocene-containing Polymers,” mar 2015.
- [97] B. Frick, J. Combet, and L. Van Eijck, “New possibilities with inelastic fixed window scans and linear motor Doppler drives on high resolution neutron backscattering spectrometers,” *Nuclear Instruments and Methods in Physics Research, Section A: Accelerators, Spectrometers, Detectors and Associated Equipment*, vol. 669, pp. 7–13, 2012.

## BIBLIOGRAPHY

---